Enabling Science through European Electron Microscopy

Third report on TEM methods applied to materials for transport

Deliverable D10.3 – version 1.2

Estimated delivery date: M48 December 2022

Actual delivery date: M49 January 2023

Lead beneficiary: KRA, TRO

Person responsible: Adam Kruk, Randii Holmestad

Deliverable type: ☒ R ☐ DEM ☐ DEC ☐ OTHER ☐ ETHICS ☐ ORDP

Dissemination level: ☒ PU ☐ CO ☐ EU-RES ☐ EU-CON ☐ EU-SEC

THIS PROJECT HAS RECEIVED FUNDING FROM THE EUROPEAN UNION'S HORIZON 2020 RESEARCH AND INNOVATION PROGRAMME UNDER GRANT AGREEMENT NO **823717**

Grant Agreement No:	823802
Funding Instrument:	Research and Innovation Actions (RIA)
Funded under:	H2020-INFRAIA-2018-1: Integrating Activities for Advanced Communities
Starting date:	01.01.2019
Duration:	54 months

Table of contents

Revision history log

Version number	Date of release	Author	Summary of changes
V0.1	10.12.2022	Adam Kruk	Preparation of the initial version of the report.
V0.2	21.12.2022	Trondheim node (Randi Holmestad Dipanwita Chatterjee, Tina Bergh, et al)	Gone through report, added parts
V0.3	21.12.2022	Adam Kruk Grzegorz Cempura Oleksandr Kryshtal	Final editing correction
V1.1	03.01.2023	Lucie Guilloteau	Amendment of the draft
V1.2	04.01.2023	Peter van Aken	Approval of the deliverable

Task 10.1: Sample preparation for materials for transport (KRA, TRO, TOU, LJU)

This task aims to implement sample preparation methods for various "difficult" materials such as Ni-based superalloys, advanced high-strength steels (AHSS), Ti, Al and Mg-based alloys and fibre-reinforced composite materials using different techniques for preparing thin artefact-free TEM lamellae.

High-quality electron transparent thin specimens are essential for state-of-art TEM/STEM investigations. This sample is necessary to examine a structural element at an atomic scale. That is why a great effort has been put into the optimization of the existing sample preparation techniques, such as tripod polishing, ion milling, FIB techniques, electro-polishing and ultramicrotomy. New techniques for preparing sensitive samples were also investigated. Finally, protocols for sample preparation were prepared and published online on the ESTEEM3 website.

Applied methods of preparing thin samples for TEM investigation in the form of thin films or lamellas:

- Correlative multiscale electron microscopy, 3D FIB-SEM tomography with detailed TEM investigation - ***targeted sample removal*** from analyzed volume.
- The aluminium lamellae preparation for in-situ heating in TEM. BF-TEM images and an SEM image (top right) of an aluminium lamella attached to a DENS chip for in-situ heating in TEM. Results from NTNU TRO.
- Electrolytic polishing of metallic specimens allows investigation of structural materials that allow for better statistics compared to FIB lamellas.

Task 10.2: Materials for Aeronautics/Aerospace (KRA, TRO, TOU)

10.2.1. Microstructural studies of nickel-based superalloy

This task presents the results of applying analytical TEM and FIB-SEM tomography techniques to perform detailed characterization (visualization in 3D, quantification and phase identification) of structural elements in various engineering materials. The KRA team investigated materials' structure and phase morphology due to their application for aeronautics, including Ni-base superalloy Inconel 718 and Allvac 718Plus; those results are described and presented below.

- This task presents the results of applying analytical TEM, FIB-SEM tomography techniques, and STEM-EDX to 3D visualization and phase identification of structural elements in various engineering materials.
- The KRA team investigates the structure of Ni-base superalloy Inconel 718 and Allvac 718Plus. The effects of post-welding heat treatment on the Microstructure of the fusion zone of the Inconel 718/Allvac718Plus welded joint was analyzed.
- The microstructural analysis was supported by the simulation of the precipitation processes carried out in the Termo-Calc software.
- Analysis of nanoparticles from binary Ag-Cu system.

Welding is an essential process in the aircraft industry, especially for IN718 and IN718plus alloys. Welding processes are used during manufacturing of structural elements and repair after service. The weldability, mechanical properties of the joint at the operating temperature (usually at high temperatures), and corrosion resistance of Ni-base alloys are generally controlled by the fusion zone's solidification behaviour and the resultant Microstructure and final mechanical properties of structural elements. The influence of a high temperature during the welding process and in the temperature conditions during the service of these elements results in the evolution of the Microstructure. In the base materials, it thereby influences the size and volume fraction of the strengthening phases; as a result, this leads to a decrease in the mechanical properties of the element due to changes in the fusion zone (FZ) and heat-affected zone (HAZ). The Inconel 718 (IN718) and its modification, ATI 718Plus® (718Plus), belong to the most used precipitation-strengthened Ni-based superalloys that are used in the aeronautic and energy industries due to their excellent creep resistance, high yield strength and exceptional oxidation behaviour at high temperatures. Those alloys exhibit good welding properties, which is very important from the manufacturing and repair points of view. Considering the continuing trend toward higher operating temperatures in turbine engines in aircraft industries, the 718Plus alloy should be an attractive replacement for the IN718. The alloy would be suitable for any static or rotating part currently made of IN718, including rings, housings, discs, blades, shafts, fasteners and structural castings.

The chemical composition of 718Plus alloy is a modification of IN718, which is modified by adding Al, Co and W in order to favour γ' phase stability, which also had the effect of stabilizing the η phase over δ. The modification mentioned above significantly improves the thermal stability of the strengthening particles γ' up to 704 °C. The precipitation of these phases results from the segregation of alloying elements, mainly Nb, to interdendritic areas. The presence of these phases causes deterioration of the mechanical properties of the alloy.

The results analysis stability of phases which are presented in the fusion zone of the Inconel 718/ATI 718Plus welding joint during isothermal holding at a temperature of 649 °C was presented. Decomposition of the Laves Phase in the Fusion Zone of the Inconel 718/ATI 718Plus® welded joint during isothermal holding at a temperature of 649 °C.

10.2.2. Microstructure of the base material IN718

For 3D visualization of strengthening particles in IN718 in as received condition, a FIB-SEM technique was employed utilizing NEON CrossBeam 40EsB (ZEISS, Germany) microscope with Ga-ion beam. In-lens, secondary- and Energy-selective Backscattered (EsB) electron images were obtained using a beam with 1.5 kV and 50 pA. In-situ milling was performed using an Ga ion beam operating at voltage-current parameters as 30 kV, 50 pA, and with a 30 µm aperture. Tomographic reconstruction was performed as follows: at first, the region of interest (ROI) was identified by SEM imaging and coated by a protective platinum layer to prevent any adverse preparation effects, such as the curtaining effect, and make the milling process more stable. The stack of 146 SEM images (image size 1024 x 768 pixels, 8-bit grayscale, stack size 113 MB) was acquired from the cross-section of the investigated sample. All the data processing, including image shift corrections, image analysis and 3D visualizations, were performed using open-source Fiji software. The same image analysis was applied for each image in the reconstructed stack, even though the contrast in some slices was slightly different. The presented approach allowed for minimizing the subjective analysis factor. The nearest-neighbourhood algorithm was used for object segmentation; thus, nearby voxels with the same and similar grey levels were assigned to one object. 3D visualization of the reconstructed volume was done using Avizo Fire 6.3 software (ThermoFisher, USA).

In **Fig.10.2.1,** a visualization in 3D of the reconstructed volume of the IN718 base material in the as-received condition after standard heat treatment for this alloy is presented. Grains differing significantly in crystallographic orientation are visualized in a different colour. Annealing twins are also seen as a parallel structure elements. **Fig. 10.2.2** presents the results of the reconstruction and visualization in 3D of the morphology and spatial distribution of γ″ precipitates being the main factor strengthening the IN718 alloy after standard heat treatment.

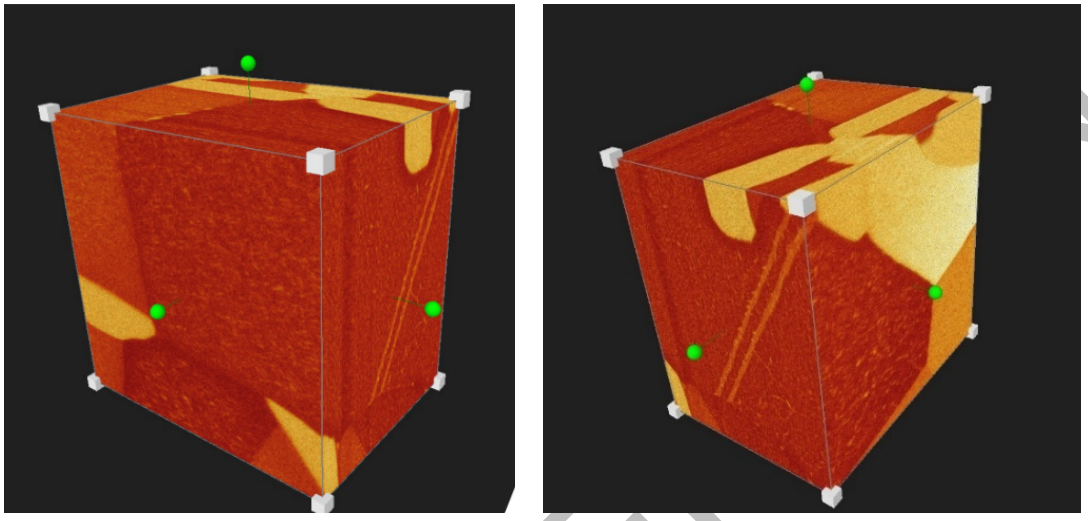

Figure 10.2.1. 3D reconstruction of the base material IN718 after a standard heat treatment for this alloy.

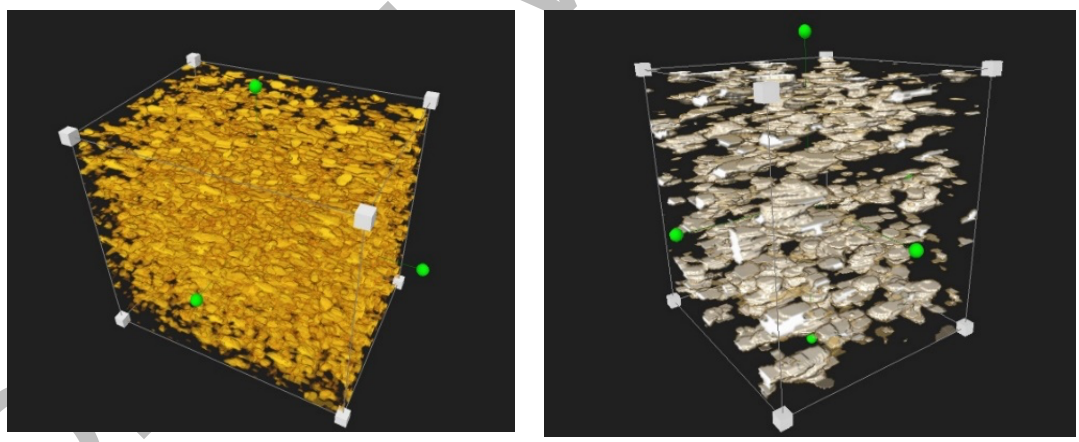

Figure 10.2.2. 3D reconstruction of the IN718 base material in as received condition, visualization of morphology, and spatial distribution of γ″ precipitates.

The results of the quantitative analysis of the volume fraction of the γ″ precipitates were carried out on 2D images and the tomographically reconstructed 3D volume. The results show excellent agreement regardless of the counting method (2D or 3D). The obtained results are shown in **Fig.10.2.3.**

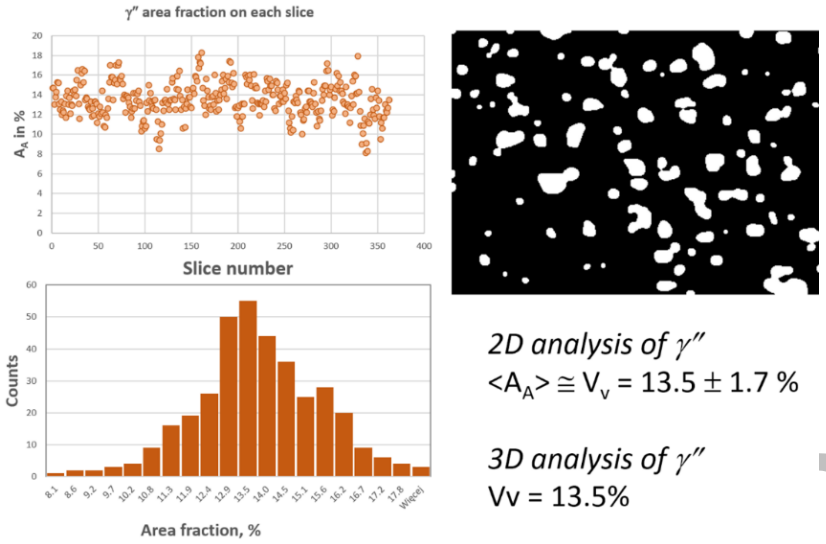

Figure 10.2.3. Results of the quantitative analysis of the volume fraction of the γ'' precipitates performed on 2D images and the tomographically reconstructed 3D volume.

10.2.3. Microstructure of the weld material

Figure 10.2.4 presents the Microstructure of the joint and as well as precipitations that were present in the interdendritic areas of the IN718/718Plus fusion zone immediately after the welding process (**Fig. 10.2.4a**) and after the different annealing durations at 649 °C (**Fig 10.2.4 b-d**). The precipitates of primary carbides NbC and Laves phase particles were observed (**Fig.10.2.4a**). There was no observed precipitation of the strengthening phases such as γ' and γ'' in either the dendritic or interdendritic areas of the weld, which was confirmed by a TEM-SAED examination. Annealing of the joint for 50 hours initiated the precipitation process of the other phases (α-Cr) both on the Laves/matrix interface and inside the Laves phase particle volume (**Fig.10.2.4.b, c**). An SEM-BSE observation confirmed the precipitations of the Cr-rich phase (**Fig.10.2.4** dark areas in the SEM-BSE images) and inside the Laves phase.

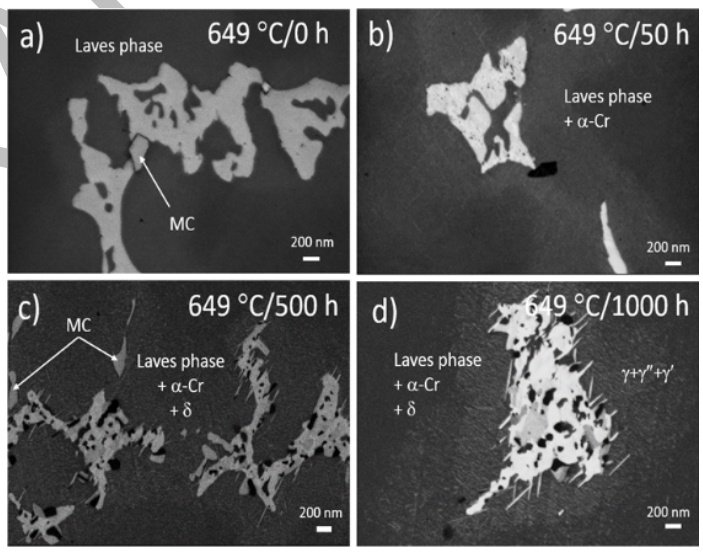

Figure 10.2.4. Evolution phase composition within the weld zone: SEM-BSE images of interdendritic areas of the IN718 / 718Plus weld joint; a) initial state after welding, after annealing at 649 °C for b) 50 h, c) 500 h, d) 1,000 h.

The distribution of selected elements in the analyzed area, which was presented on elemental maps, provided qualitative information about the distribution of elements (**Fig.10.2.5**). The results show that elements such as Nb, Mo, Ti and C segregated strongly to the interdendritic regions, unlike Cr, whose concentration was higher in the dendritic regions. This segregation, especially of Nb, leads to the precipitation of Laves phases in these regions.

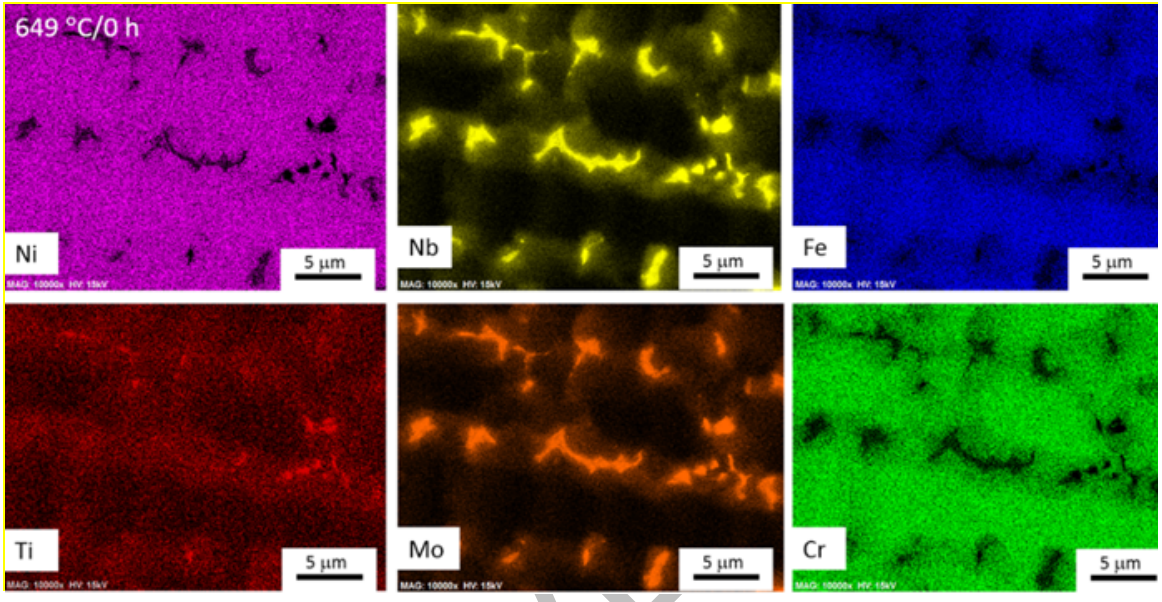

Figure 10.2.5. Qualitative SEM-EDX elemental maps of selected elements for the weld area of the IN718/ 718Plus welded joint directly after welding without any additional heat treatment.

A STEM-HAADF analysis performed in the interdendritic area of the fusion zone of the IN718/718Plus joint after annealing at a temperature of 649 °C for 50 hours revealed complex shape Laves phase particle with areas of different contrasts inside the particle (**Fig. 10.2.6**).

The TEM image of the Laves phase showed numerous precipitates with a plate-like morphology with a periodic contrast on the interphase boundary (**Fig.10.2.6e**). This contrast fluctuation resulted from a lattice mismatch between the precipitated lamellar phase and the matrix (Laves phase). In the Laves phase particle, the HAADF images exhibited small areas of a darker grey level which are precipitates of particles of the Cr-rich phase (**Fig.10.2.6c**). **Figure 10.2.6f** shows the δ phase plates that were growing into the matrix area surrounding the Laves phase.

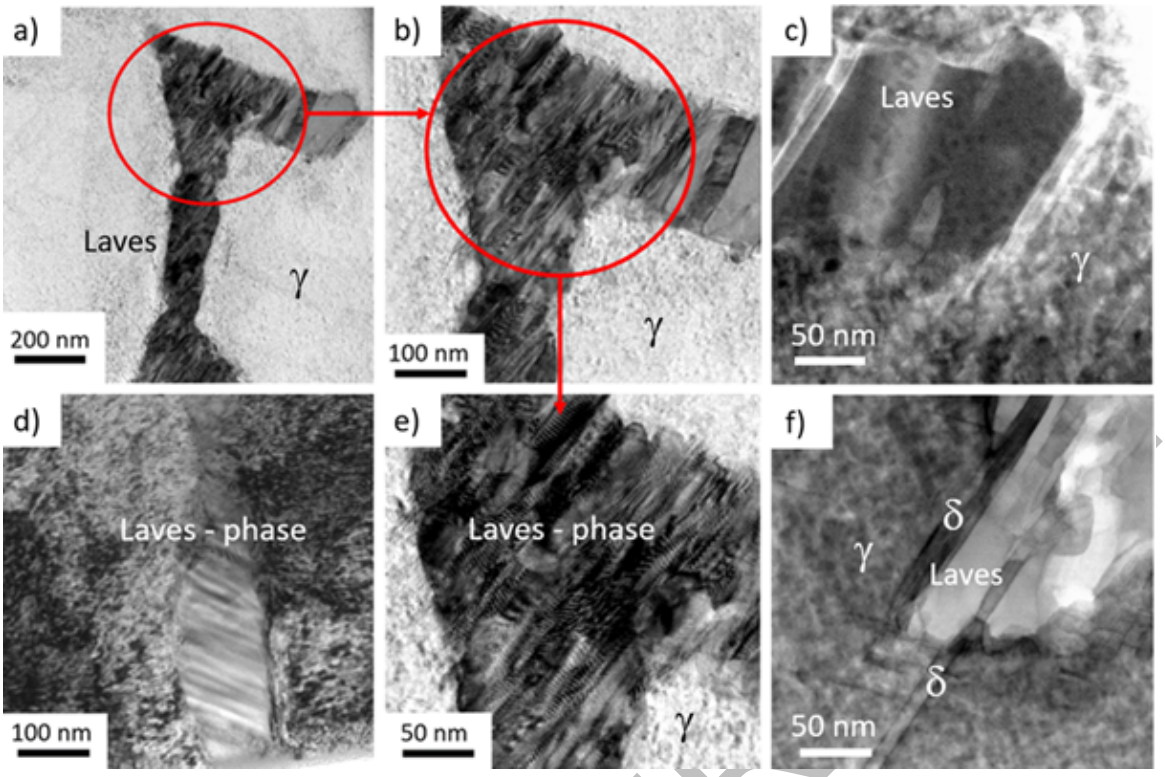

Figure 10.2.6. STEM-HAADF images from the interdendritic area of the welded joint IN718/718Plus after annealing at the temperature of 649 °C for 50 hours. a) Laves phase particle shape with visible areas of different contrast. b) Enlarged fragment of image a). c) Laves phase precipitates with contrast from the particles precipitated inside the Laves phase. d) Another area with a Laves phase particle with visible contrast bands. e) Enlarged fragment of a Laves phase particle with ordered and directed oriented defects. f) The plate-like δ particles inside the Laves phase.

10.2.4. Microstructure of the weld material, decomposition of the Laves phase

Annealing the welded joint for 50 hours resulted in a complex precipitation process for the different structural elements on the phase boundary (Laves/γ) and within the Laves particle. The relevant STEM-EDX maps of the distribution of the selected elements are shown in **Fig.10.2.7**. Numerous Cr-enriched precipitates were present inside the Laves phase.

The more complex precipitates consisted of Cr-rich particles and secondary (Nb,Ti)C carbides (**Fig. 10.2.7a**). The presence of regions with a plate-like morphology, which were depleted in Mo and Cr but contained a higher concentration of Nb and Ni suggests that there are the initial stages of the δ phase precipitation inside the Laves phase particle. The observed precipitates had a different chemical composition, resulting in changes in the STEM-HAADF image contrast (Z-contrast). **Fig.10.2.7b**, a composite of the maps for Cr, Nb and Ti, shows the differentiation of the chemical composition and precipitations of the other phases that had precipitated inside the Laves phase. A phase was identified based on SAED, HRSTEM-HAADF and was supported by a STEM-EDX analysis.

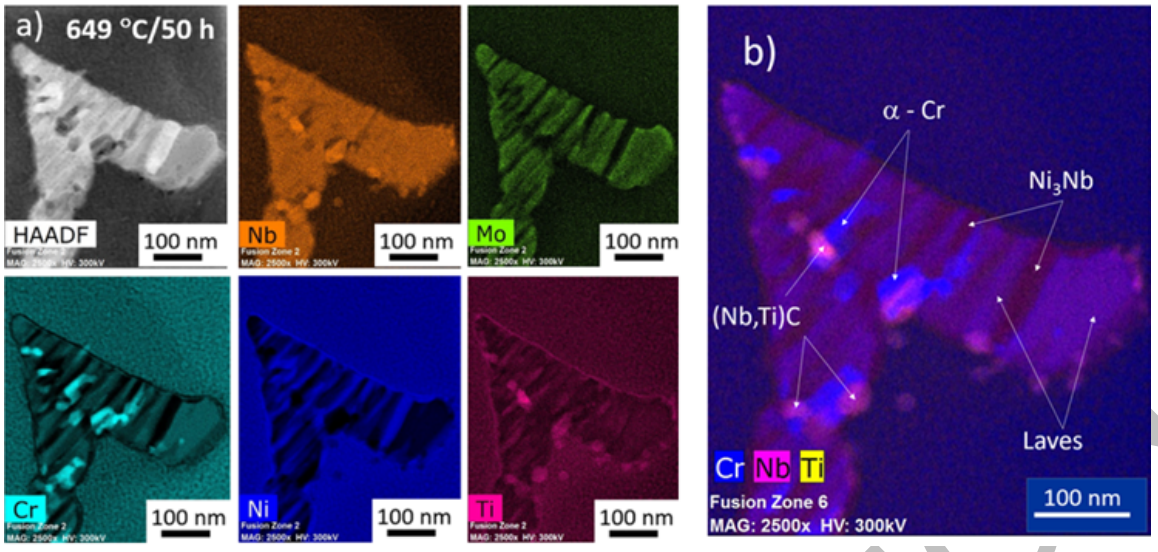

Figure 10.2.7. Qualitative STEM-EDX maps of the distribution of selected elements from the Laves phase area in the weld of the IN718/718Plus weld joint subjected to annealing after the welding process for 50 hours at a temperature of 649 °C. a) STEM-HAADF image and qualitative STEM-EDX maps of selected elements for the weld area with Laves phase precipitates. b) Qualitative maps of Cr, Nb and Ti with marked secondary precipitates of other phases.

The STEM-EDX analysis (**Fig.10.2.8**) allowed for determination of the chemical composition in different areas of the Laves phase and thus allowed the identification of different phases precipitates in these areas (Laves, γ, δ, α-Cr). Identification was performed based on TEM-SAED diffraction analysis and HRSTEM-HAADF high-resolution analysis.

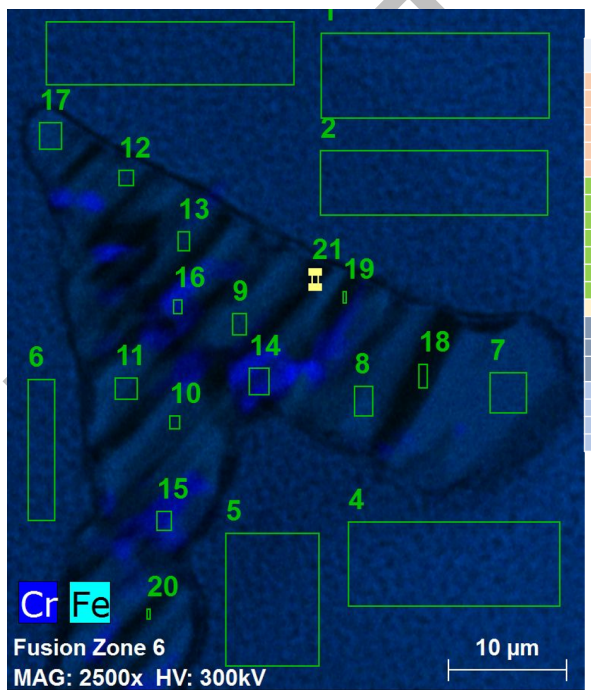

Atomic-% (norm.)	Al-K	Ni-KA	Cr-KA	Fe-KA	Nb-KA	Ti-KA	Mo-KA	W-LA	Zr-KA	Co-KA
1	0.3	57.12	16.63	11.88	5.31	1.04	2.13	0.02	0.85	4.72
2	0.3	57.31	16	11.44	6.17	1.11	1.98	0.03	0.95	4.7
3	0.33	57.34	15.18	10.75	7.58	1.23	1.81	0.02	1.09	4.66
4	0.39	57.35	17.28	12.21	4.51	1.03	1.86	0.02	0.75	4.61
5	0.51	59.16	14.78	10.25	7.04	1.4	1.51	0.02	1.04	4.29
6	0.52	58.07	15.14	10.6	7.38	1.24	1.54	0.02	1.11	4.39
7	0.2	33.46	16	12.77	21.95	1.2	3.56	0.03	2.94	7.9
8	0.25	34.33	14.54	12.51	21.69	0.96	4.98	0.05	2.94	7.74
9	0.24	41.1	11.49	10.95	21.26	0.88	4.16	0.06	2.92	6.94
10	0.2	45.95	10.39	8.95	21.02	1.11	3.05	0.05	2.87	6.41
11	0.35	41.81	11.67	10.78	20.62	1.09	3.8	0.04	2.92	6.93
12	0.3	42.02	11.16	10.37	21.15	0.62	4.23	0.08	2.99	7.09
13	0.36	45.16	10.42	9.66	19.67	1.08	4.47	0.01	2.54	6.62
14	0.25	18.14	31.62	4.12	33.29	3.36	2.15	0.39	4.36	2.32
15	0.29	32.76	35.21	5.16	18.15	0.78	1.98	0	2.55	3.11
16	0.32	36.97	32.95	5.13	14.64	0.89	3.91	0	2.07	3.12
17	0.21	31.94	15.4	12.91	22.2	0.69	5.85	0.04	2.93	7.82
18	0.34	65.35	3.09	4.03	18.62	1.58	0.21	0.04	2.49	4.26
19	0.21	64.17	3.51	4.08	20.18	0.56	0	0.18	2.59	4.53
20	0.08	61.12	4.41	5.39	19.78	1.53	0.45	0.02	2.31	4.9
21	0.33	62.78	3.91	4.13	20.79	1.16	0.59	0.07	2.7	3.54

	γ
	Laves
	α - Cr
	δ

Figure 10.2.8. Marked Areas where the STEM-EDX analysis of the chemical composition of a single Laves phase precipitate and the adjacent matrix was carried out and results of the chemical microanalisys (right side).

The progress of the transformation of the Laves phase to other phases is visible on the sample after longer annealing times. For the sample heat treated for 500 hours, the Laves phase transformed into a complex conglomerate of different phases, which is well documented in **Fig.10.2.9** and the Cr, Nb, Mo and Ti quality maps.

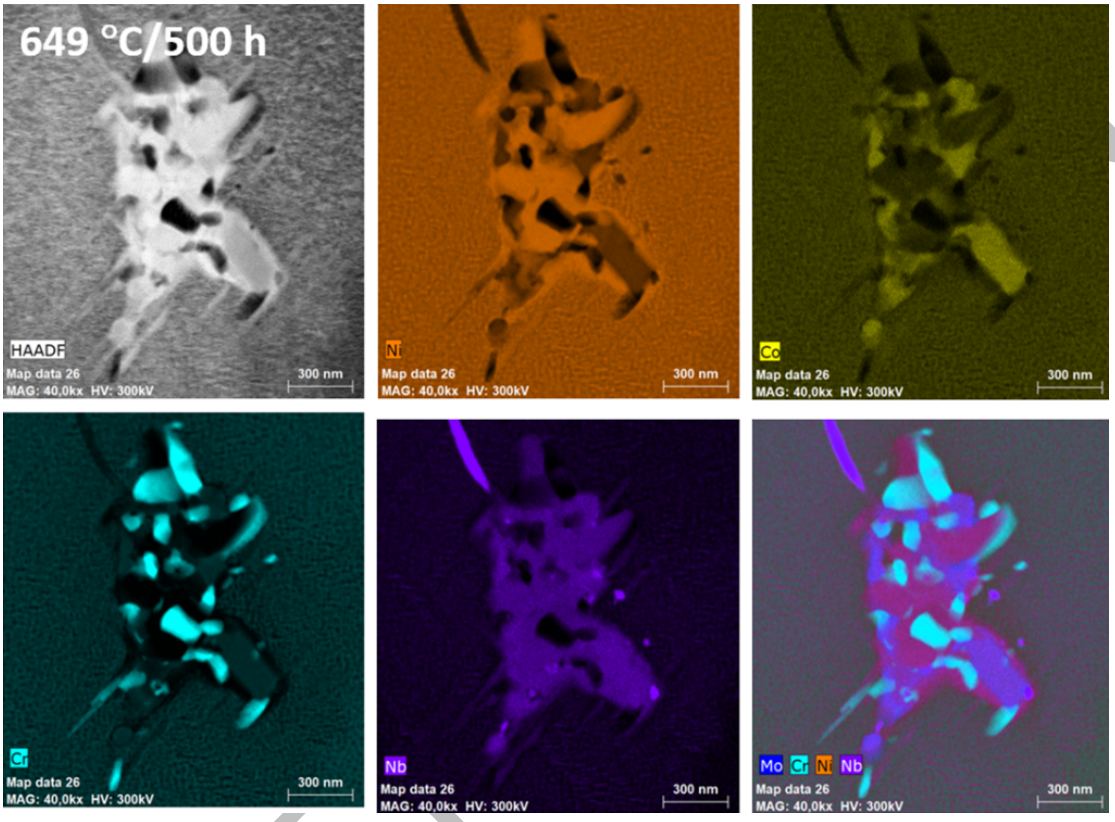

Figure 10.2.9. Qualitative STEM-EDX maps of the distribution of selected elements from the Laves phase area in the IN718/718Plus weld joint subjected to annealing after the welding process for 500 hours at a temperature of 649 °C.

Extension of the annealing time leads to further breakdown of the Laves phase. A plate-like δ phase precipitate that was growing from the Laves phase and growing into the $\gamma + \gamma'' + \gamma'$ interdendritic areas was observed. The plate-like δ phase that was growing out of the Laves phase had the same crystallographic orientation due to crystallographic relationship between the Laves phase and the γ matrix. **Figure 10.2.10** shows selected SEM-BSE images from the weld areas of the IN718/718Plus welded joint after annealing for 1,000 hours at a temperature of 649 °C. Precipitation of the Nb-rich secondary carbides was observed in the Laves phase. Thus, the decay reaction can be written as Laves $\rightarrow$ Laves + γ+ α-Cr + secondary MC(II).

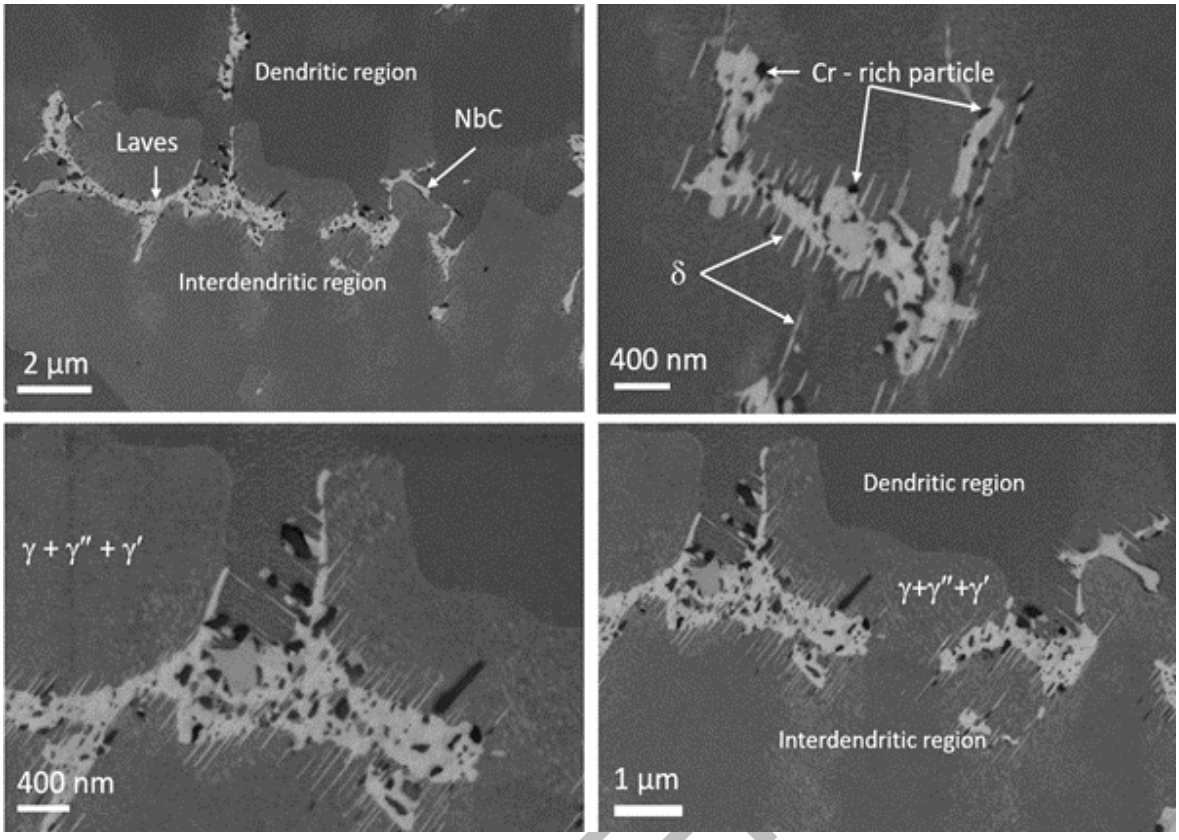

Figure 10.2.10. Chosen SEM-BSE images from the weld areas of the IN718/718Plus, after annealing for 1,000 hours at a temperature of 649 °C.

Figure 10.2.11 shows the 3D visualization of the tomographically reconstructed sample volume equal to 70.8 µm^3 from the interdendritic area of the IN718/718Plus weld joint. Investigated volume contained the Laves phase precipitates. Nucleation of the α-Cr phase occurred on Laves /γ boundaries – even inside a γ + Laves eutectic. 3D imaging allowed us to visualize a-Cr precipitates' morphology and measure their spatial distribution. The precipitates are similar in size, and their average diameter is <D> = 104 nm. **Fig.10.2.12**. 3D visualization of the tomographically reconstructed volume of 2.94 µm^3 of the IN718/718Plus weld area heat-treated for 50 h at 649 °C, containing the Laves phase precipitate and primary carbides of the welded joint. The voxel size: was 1.5 x 1.5 x 3 nm. A shorter annealing time reveals smaller precipitates of the α-Cr phase with an average diameter <D> = 28 nm. The 3D reconstruction also shows the morphology and size of the MC type's primary carbides occurring in the weld's interdendritic area.

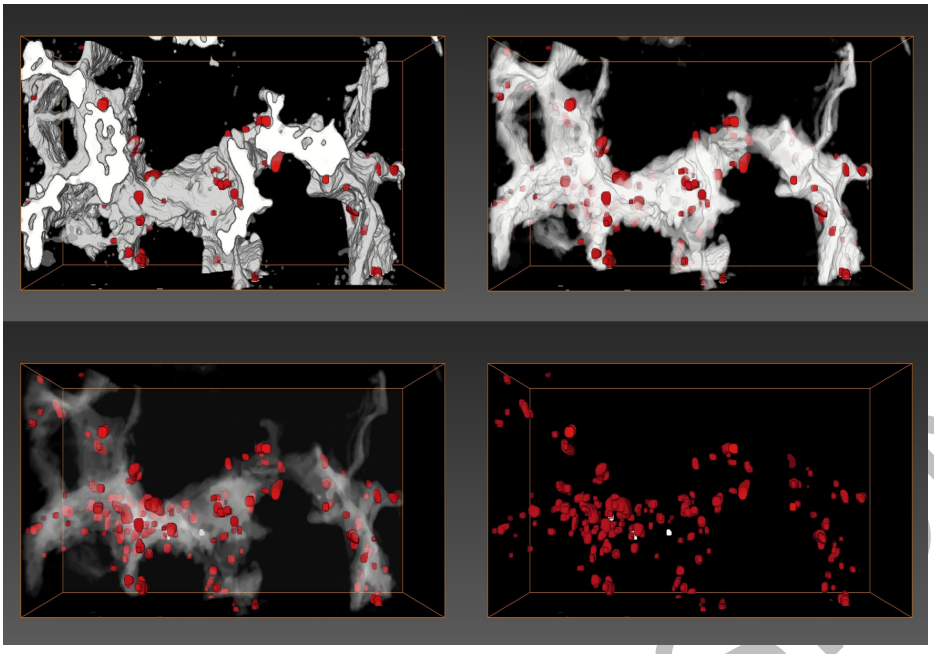

Figure 10.2.11. 3D reconstruction of the fusion zone, post-welded heat treated for 500 h at 649 °C. Nucleation of the α-Cr phase occurred on Laves/γ boundaries – even inside a γ + Laves eutectic. The reconstructed volume: 70.8 μm^{3,}, voxel size: 13 x 13 x 13 nm.

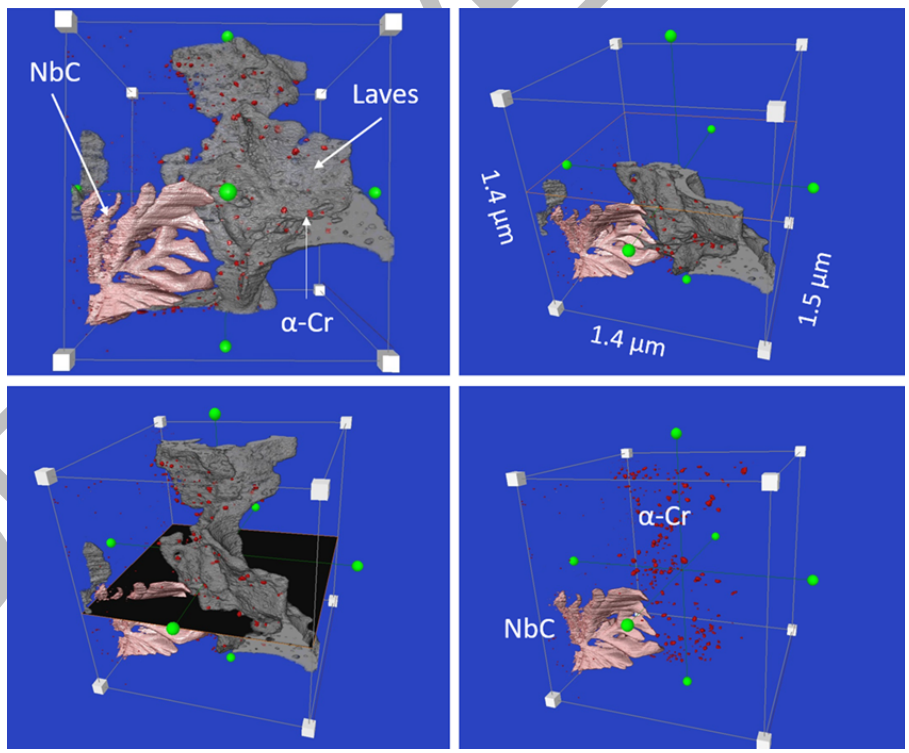

Figure 10.2.12. 3D visualization of the tomographically reconstructed volume of 2.94 μm^3 of the IN718/718Plus weld area, heat-treated for 50 h at 649 °C, containing the Laves phase precipitate and primary carbides within the welded joint. The voxel size: 1.5 x 1.5 x 3 nm.

High-resolution TEM studies showed the presence of a mismatch in the distribution of crystallographic planes between the δ phase plate and the Laves phase. The system compensates for the mismatch by introducing a linear defect, a dislocation with an edge orientation. The system of edge dislocations can compensate for such a mismatch at the interphase boundary, a semi-coherent δ/Laves interface is formed. A similar type of interface also occurred for the δ phase plate, which grew into the γ phase matrix surrounding the Laves phase. The mismatch analysis in the interface was based on the digital analysis of the high-resolution HRSTEM-HAADF image using the inverse FFT. The result of geometric phase analysis calculating the dilatation between δ/γ phases in the HRSTEM image was made in the Strain ++ software. The simulation of HAADF images were performed in the JEMS software for δ phase with ZA [4 0 3] and for γ phase with ZA [1 1 1], the results are presented in **Fig.10.2.13**.

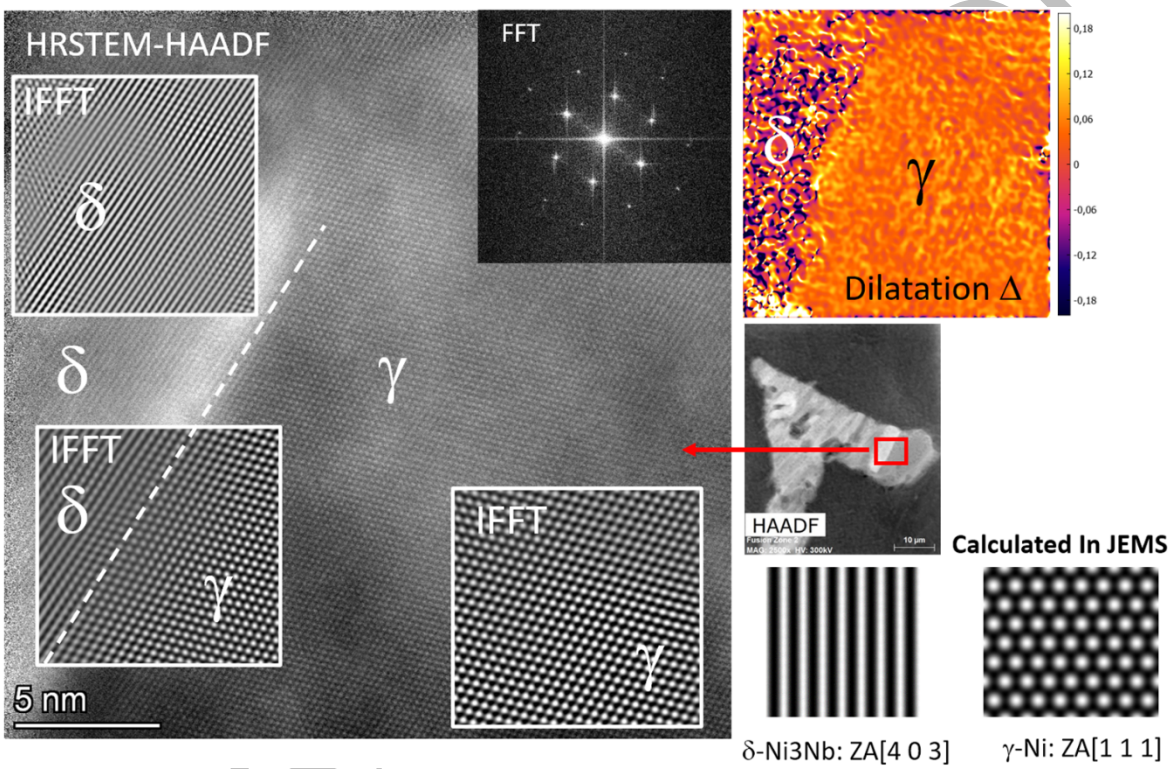

Figure 10.2.13. Precipitation of the Laves phase with the marked area containing the δ phase plate. High-resolution analysis of the δ phase plate, growing from the Laves phase into the γ matrix in the fusion zone of the IN718/718Plus weld joint after annealing for 50 hours at 649 °C.

Figure 10.2.14 shows the method of revealing the mismatch in the distribution of planes in the δ/γ interfacial pot. The use of IFFT from selected reflections allowed to show the places of mismatch in the arrangement of atomic planes in both phases. Since the differences in the lengths of the reciprocal lattice vectors are slight for both phases, performing the inverse transform from the selected reflections, IFFT from two very close to each other reflections for both phases was performed. Hence, it was possible to obtain an image that results from interference, the mismatches are visible and located mainly at the interface.

As was confirmed by the HRTEM analysis, the δ phase possesses a high density of structural defects – stacking faults, which caused crystallographic lattice distortions. The δ/γ phase boundary had a semi-coherent nature due to the high mismatch that was compensated by edge dislocations within the δ

phase and at the δ/γ phase boundary and because there was no fully periodic distribution of the dislocation.

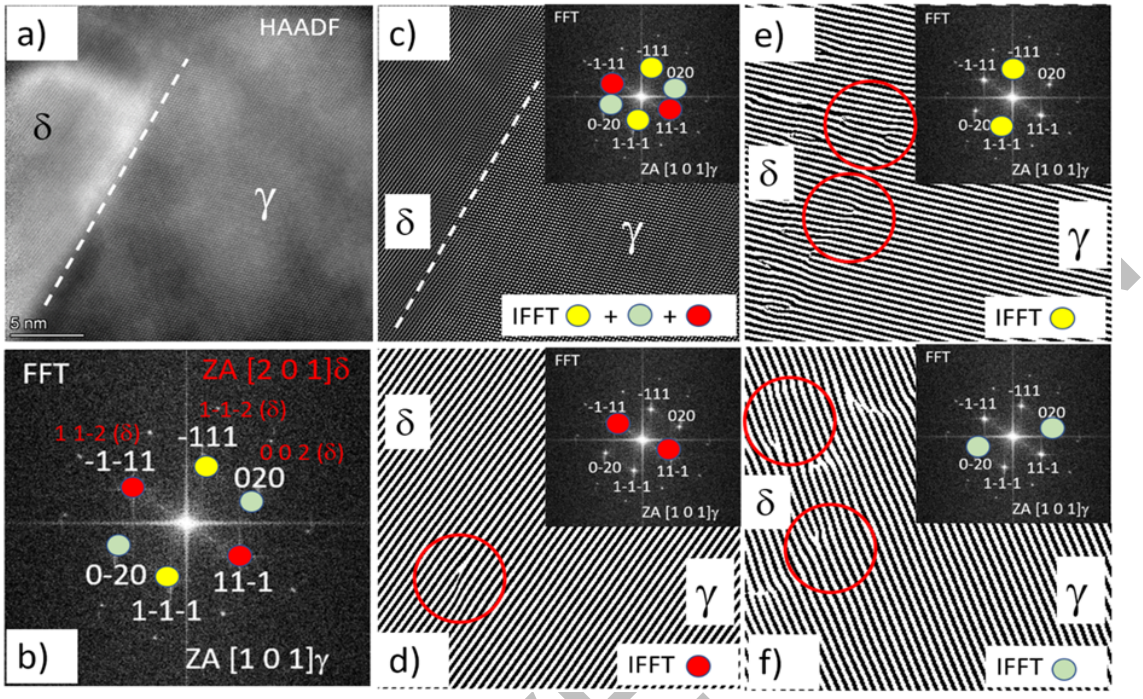

Figure 10.2.14. Results of high-resolution investigations of the phase boundary between δ phase precipitating within the γ matrix. a) STEM-HAADF of the phase boundary between the δ, that grows inside the matrix (γ). b) Power spectrum of FFT from the boundaries with marked reflections selected for γ and δ phase. c) IFFT image based on reciprocal space g vectors (-1 -1 1) + (-1 1 1) + (0 2 0) for the γ, zone axis [1 0 1]. d-f – IFFT images for corresponding reflections, marked with red and green dots.

Figure 10.2.15 presents a STEM-HAADF analysis of the boundaries between the Laves and the δ phase precipitates inside the Laves phase. As seen on the STEM-BF **(Fig.10.2.15b, c**), there were periodic changes in the contrast. Those changes resulted from the stress fields due to the mismatch of the crystallographic planes of both phases. The bottom image in **Fig.10.2.15** shows the places of mismatch in the distribution of atomic planes in both phases (δ and Laves). These spots are visible as darker areas in the STEM-HAADF image. The contrast oscillation indicates a specific order in their arrangement, such an effect is caused by the introduction of an order in the arrangement of linear defects compensating for the mismatch of atomic planes in the interphase boundary. **Figure 10.2.15** shows the power spectrum of the FFT from the Laves/δ phase boundary area. Those images are almost identical, and the vector **g**(-2 2 1) of the reciprocal space for the Laves phase was common for both phases. The spots in reciprocal space (FFT) were selected to show the arrangement of the (-2 2 1) planes within the investigated area (**Fig. 10.2.15**).

A similar analysis for another area within the Laves phase precipitate is shown in **Fig.10.2.16**. Also, areas of mismatch of atomic planes are visible as places of different contrast.

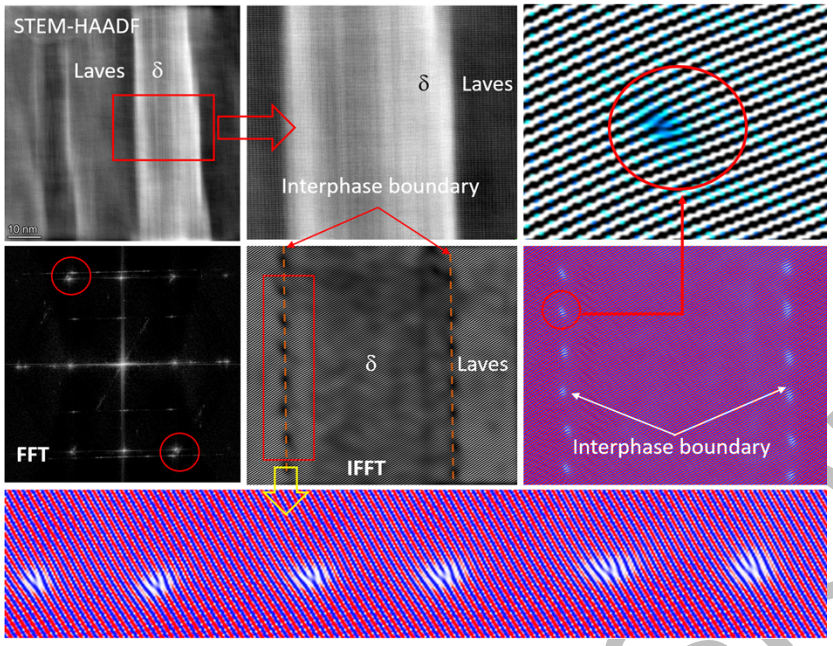

Figure 10.2.15. High-resolution analysis of the Laves/δ interphase boundary from the weld area of the IN718/718Plus welded joint after annealing for 50 hours at a temperature of 649 °C. High-resolution analysis of the Laves/δ interphase boundary from the weld area of the IN718/718Plus welded joint after annealing for 50 hours at a temperature of 649 °C. The delta phase nucleates in Laves phase particle on which high-resolution analysis was performed. HRSTEM-HAADF image after digital filtering using FFT bandpass filtration. Application of IFFT for visualization of interphase Laves/δ phase boundary. The dislocation system compensates for the network mismatch, which means we deal with a semi-coherent interphase boundary.

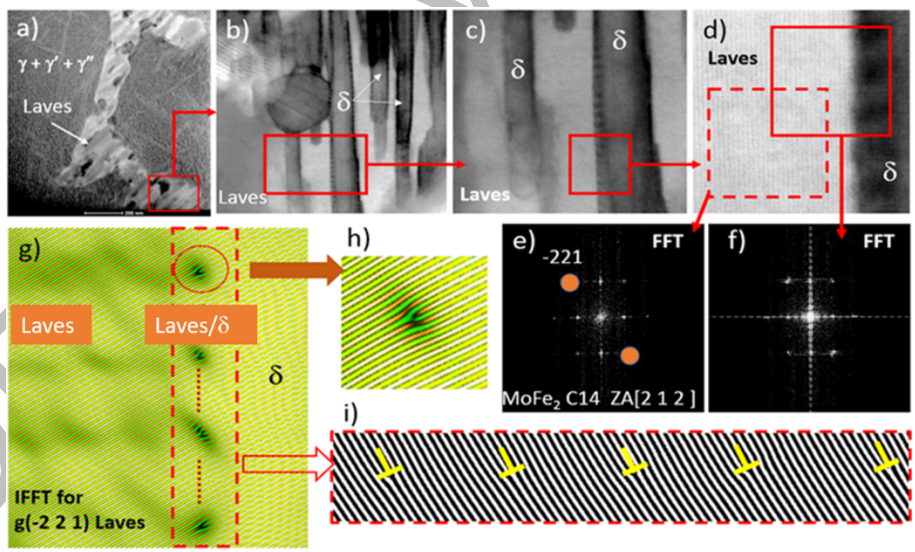

Figure 10.2.16. HRSTEM analysis of the phase boundaries between precipitate of the plate of δ, that precipitates inside Laves phase. a) HAADF image of Laves phase with the marked area, selected for further analysis. b) magnified area of (A), visible plate-like precipitates of δ phase inside Laves phase. c) – magnified image (BF-STEM), visible contrast oscillation at the Laves/δ phase boundaries. d) HR-STEM image of the interfaces boundary and contrast oscillation. Red squares indicate the area of FFT analysis. e-f – power spectra of FFT from the marked areas. g) IFFT, created on the g[-2 2 1] vector of the Laves phase, visible network mismatch – presented in detail on (h). Arrangement of planes at the boundaries of Laves/δ, with dislocation that compensate for the lattice mismatch.

Figure 10.2.17 presents the results of a high-resolution analysis of the STEM-HAADF images of the Laves phase precipitate in the weld zone of the IN718/718Plus weld joint that was annealed for 50 hours at a temperature of 649 °C. **Figure 10.2.17**a shows a part of the Laves phase particle on which the STEM-HAADF high-resolution analysis was performed. HRSTEM-HAADF image after the bandpass filtration is presented in **Fig.10.2.17c**. **Figure 10.2.17d** shows the 2D power spectra image of the FFT transformation with the marked vectors of the reciprocal space corresponding to the zone axis [2 1 2] indicated for the $MoFe_2$ C14 prototype of the Laves phase. **Figure 10.2.17f** shows the HAADF image that was calculated in the JEMS software for the Laves phase zone axis [2 1 2]. This image is similar to the filtered image that is shown in **Fig. 10.2.17e**.

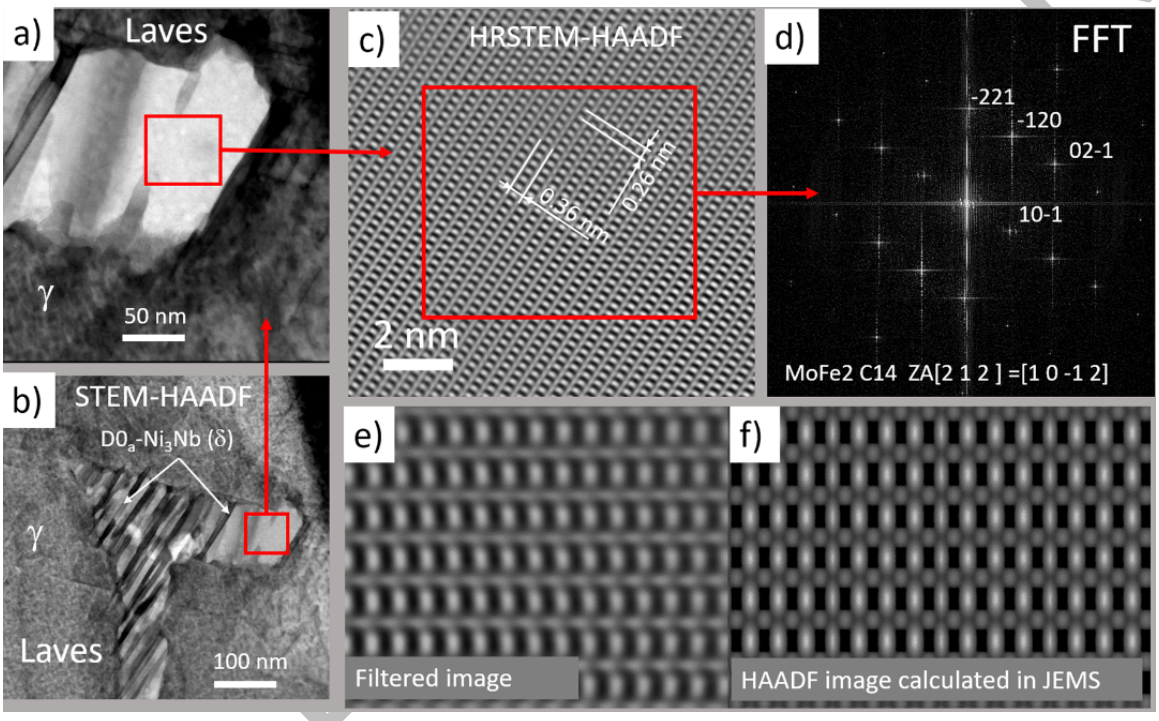

Figure 10.2.17. High-resolution analysis of the Laves phase from the weld area of the IN718/718Plus welded joint after annealing for 50 hours at a temperature of 649 °C. a) Laves phase particle on which high-resolution analysis was performed. b) Precipitate of the Laves phase with the area marked for further analysis. c) HRSTEM-HAADF image after digital filtering using FFT bandpass filtration. d) Image of the FFT transform with the marked reciprocal lattice vectors corresponding to the respective interplanar distance. e) Enlarged fragment of the image from c). f) Simulated HAADF image.

The high-resolution TEM images from the Laves phase showed the occurrence of a mismatch in the atomic plane distribution between the δ-phase plate and the Laves phase. The edge dislocations arrangement compensated for this mismatch in the interphase boundary; hence, there was a semi-coherent δ/Laves boundary. A similar type of interphase boundary also occurred in the case of the δ-phase plate that was growing into the γ-phase matrix surrounding the Laves phase.

10.2.5. Phase separation mechanism and atomic mixing patterns in AgCu nanoparticles

Modern technologies stimulate quest for multicomponent nanosized materials with improved properties, which are ultimately defined by the atomic arrangement and interphase interactions in the nanomaterial. Here we present the results of the experimental study of the formation of solid solutions in Ag-Cu nanoparticles using in situ TEM techniques.

The Ag-Cu nanoparticles with the eutectic ratio of components were formed on amorphous carbon film by the PVD technique. Electron diffraction, HAADF-STEM imaging, energy dispersive X-ray spectroscopy (EDX) chemical element mapping, and electron energy loss (EEL) spectral imaging (SI) were used for characterization of mixing patterns and composition of phases in AgCu nanoparticles down to the atomic level. A probe-corrected FEI Titan G2 60-300 TEM operating at 300 kV was used in the study. The microscope was equipped with Wildfire D6 double-tilt heating holder (DENSsolutions), Gatan Image Filter (model 966), and ChemiSTEM™ EDX system. As a rule, the temperature of the sample was incremented in 50°C steps between 25°C and 750°C.

Figure 10.2.18 shows HAADF-STEM images of Ag-Cu films of different thicknesses (with a different mean size of nanoparticles) after annealing. Janus-like and single-phase nanoparticles were firmly detected in the Z-contrast images due to a difference in the atomic number of Ag (Z=47) and Cu (Z=29). Janus morphology, consisting of Ag- and Cu-rich phases, dominated in nanoparticles with a size larger than ~8 nm. The dihedral angles at a three-phase junction in Janus nanoparticles varied widely due to different volume fractions of the phases, size, and combinations of surface and interfacial energies. As a result, “ideal” Janus nanoparticles with two halves separated by a flat interface along a diameter, “side-segregated”, and “crescent-like” Janus structures were observed (**Fig.10.2.18 a** and **Fig.10.2.19 a,b**). Careful analysis of high-resolution images revealed that α/β interfaces was preferentially coincident with the (111) planes of silver (**Fig.10.2.19 a,b**), which are likely provide the lowest energy path for copper segregation.

On the other hand, the nanoparticles with a size below ~8 nm were mostly single-phase AgCu alloy (**Figure 10.2.18 b**). Figure 2c exemplifies the HAADF-STEM image of alloy nanoparticles with a random mixture of Cu and Ag atoms. EDX spectrum from this nanoparticle (not is shown here) gave about 30 wt% of Cu, which is close to the as-deposited ratio of metals. Hence, Cu and Ag completely dissolved in nanoparticles with a size below a critical one, which was 8 nm in our case.

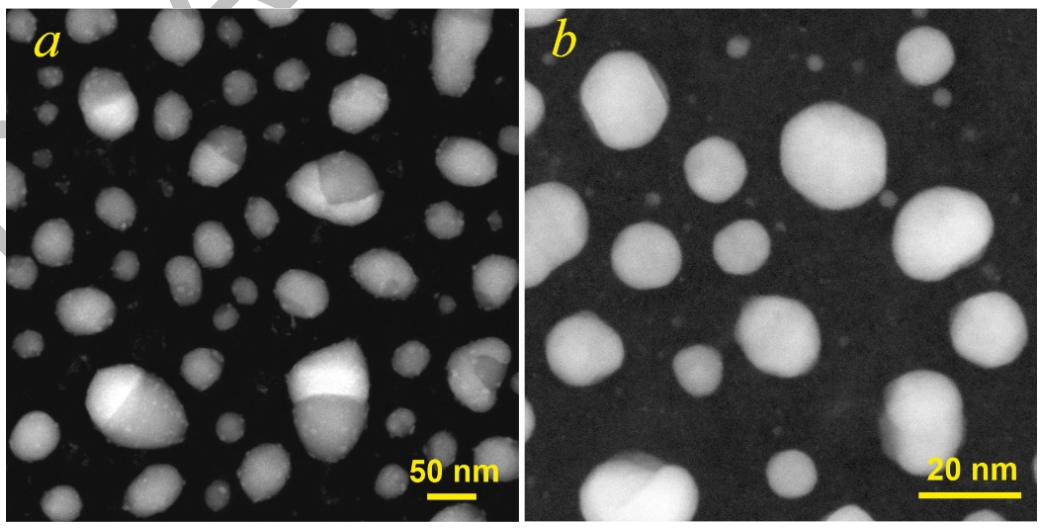

Figure 10.2.18. HAADF-STEM images of Ag-Ge film with a mass thickness of 7 nm (a) and 2.7 nm (b) after a thermal treatment.

In summary, a gradual transition from Janus-like to homogeneous mixing pattern was observed in Ag-Cu nanoparticles (28 wt.% Cu) with a decrease in their size.

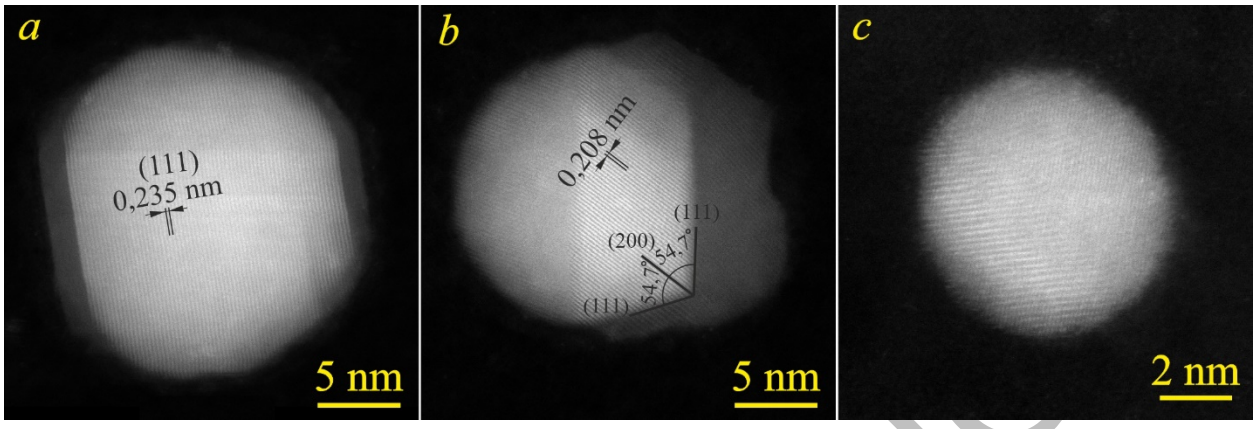

Figure 10.2.19. High-resolution HAADF-STEM images of phase-separated (a, b) and single-phase I Ag-Cu nanoparticles.

Figure 10.2.20 shows the HAADF STEM image of partly unmixed Ag-Cu nanoparticles, and the corresponding EELS component distribution map acquired at 300kV. The side-segregated Janus nanoparticles are revealed by **Fig. 10.2.20a** and **b**. At the same time, **Figure 10.2.20c** shows a relative composition map, and it proved the Cu skin in the outmost layer of Ag-rich alloy. The thickness of the Cu skin was varied over the particle from 0.3 to 0.6 nm, which was one or two pixels in size. A model-based relative quantification of the EEL spectra showed that the skin was almost pure Cu. Therefore, segregation of Cu to the surface of Ag-rich phase was revealed in partly unmixed AgCu nanoparticles.

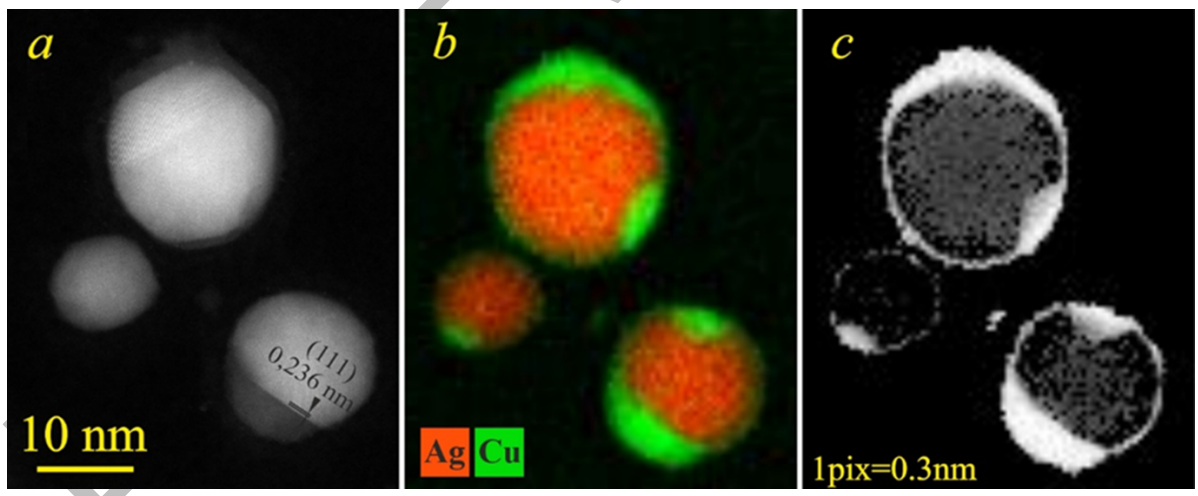

Figure 10.2.20. HAADF STEM image of the Ag-Cu binary nanoparticles at 300°C (a), corresponding EELS composite map of Ag and Cu (b), and Cu relative composition map (c).

To unravel the nature of terminal temperature, which limits the existence of AgCu alloy nanoparticles in a vacuum, we assessed the composition of the evaporated phase by analyzing overall composition and volume of a single nanoparticle before and after annealing to evaporation temperature. We used *in situ* heating TEM approach to characterize the very same nanoparticle.

Figure 10.2.21 shows the Janus nanoparticle, which was used in the analysis. The nanoparticle was annealed to 600°C to reach an equilibrium shape (**Fig. 10.2.21a**), followed by annealing to evaporation temperature of 750°C (**Fig. 10.2.21d**). To reconstruct the volume of the nanoparticle, one needs to know its 3D shape, which is challenging from 2D TEM images. Therefore, the EEL SI technique was used to assess the height of the nanoparticle and the size of the wetting zone. In this technique, the focused electron beam scans over a selected region, and the low-loss EEL spectrum is acquired at each raster point. The relative thickness t/λ (where t was the thickness, and λ was the mean free path of the electron) was assessed by using a log-ratio method from the ratio of the zero-loss electrons to the total transmitted intensity [1]. After the removal of the substrate component, the thickness map of the AgCu nanoparticle was assessed (**Fig. 10.2.21b**). We used the mean free path of the electron λ = 137 nm for Cu and λ = 132 nm for AgCu alloy, according to Jakubovski [2].

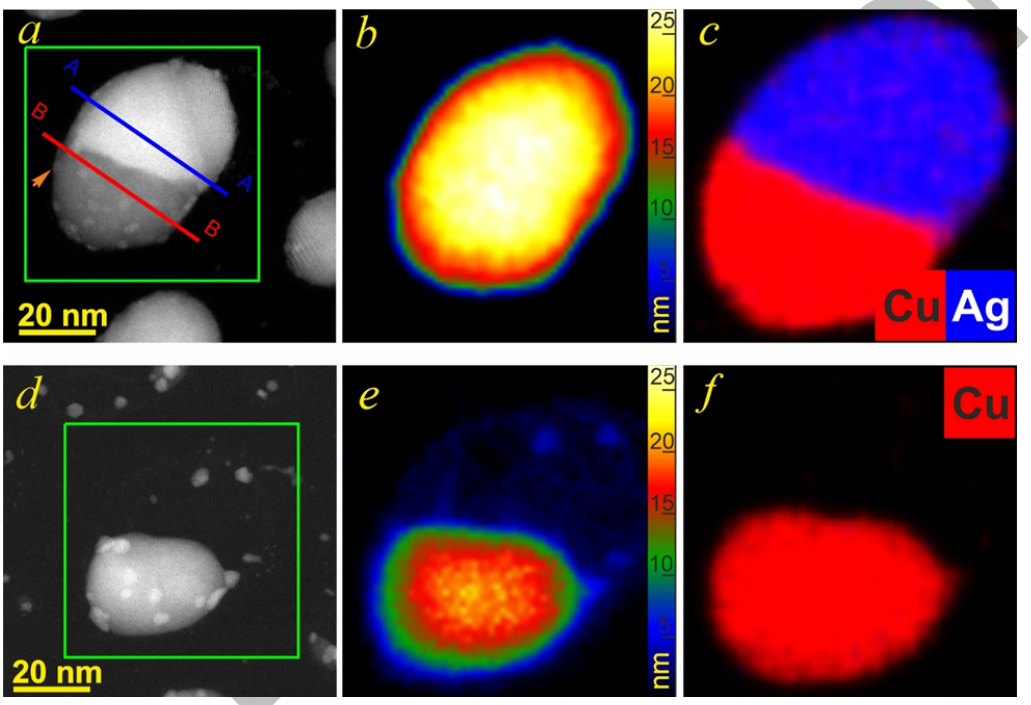

Figure 10.2.21. HAADF-STEM images of Ag-Cu nanoparticles annealed to 600°C (a) and 750ºC (d) along with false-colour thickness maps (b, e) and EDX composite maps (c) of Cu (red) and Ag (blue) acquired from the regions marked by green rectangles. AA and BB lines show the position of cross-sections, which were used for assessing the parameters of the phases. Arrow indicates CuO nanoparticle.

Table 10.2.1 accumulates the measured parameters of the nanoparticle under study. The width and length of Ag and Cu domains were measured from images, the composition was assessed from EDX spectra, and the height was determined from EELS data.

Since the height of the particle was higher than a half of the width, then in the first approximation we assumed that the AgCu nanoparticle had a shape of a truncated ellipsoid with the interphase boundary lying along the plane normal to the substrate. The volume of the truncated ellipsoid was assessed using the expression $V = \frac{1}{3}\pi abc(3 - \frac{h}{c})\frac{h^2}{c^2}$, where a, b and c are the semiaxes of the ellipsoid, and h is the height of its cap. In our case, a = d/2, b = l, h = H. However, to correctly reconstruct the shape of the ellipsoid, one needs to know the semiaxis c, which could be determined from the contact angle or the size of the wetting zone (**Fig.10.2.22a**).

Table 10.2.1. Parameters of the Ag-Cu nanoparticle (**Fig. 21a, d**), were determined from the HAADF-STEM images, ELLS, and EDX data.

	Before		After
Parameter	**Ag side**	**Cu side**	**Cu**
Content of Cu, wt%	7.5	100	100
Width *d*, nm	37.6	36	26
Length *l*, nm	29.4	24.6	36
Height *H*, nm	27	27	23
Diameter of the contact area, z, nm	26	21	23
Θ, degree	147	132	148
Volume *V*, nm^3	16 812	13 914	12 266

We were inspired by photometric approach, which was used in the past for measuring wetting angle of nanoparticles from TEM photographic plates. The thickness of a nanoparticle has two distinct regions along the diameter. Thus, in an area I of nanoparticle (in **Fig. 10.2.22a**), the thickness shows significant variation along x-axis. In contrast, the thickness in region II is almost constant. Therefore, the slope of the first derivative of the height must have an inflection point at the triple point. **Figure 10.2.22c** and d show the dh/dx plots along the A-A (a) and B-B (b) cross-sections shown in **Figure 10.2.21**. The inflection points of the curve allow one to measure the diameter of the wetting zone z. As a result, the semiaxis c and the contact angle Θ were determined for the Ag and Cu domains of the nanoparticle under study (**Table 10.2.1**). With these data, the volume of Ag and Cu domains was calculated, and the mass of the AgCu nanoparticle mAgCu = 2.98648·10-16 g was obtained. We used density values 10.455 and 8.92 g/cm3 for Ag-7.5Wt%Cu alloy and Cu, respectively.

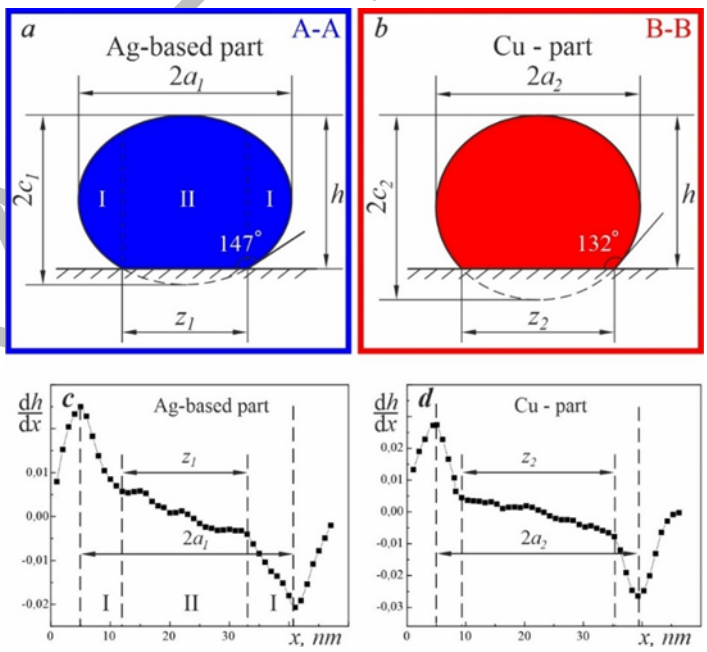

Figure 10.2.22. Schematic view of cross sections A-A (a) and B-B (b) of Ag and Cu domains. (c and d) are derivatives of EELS SI data along the corresponding cross-sections.

The shape and volume of the nanoparticle, which was annealed to 750 ºC (**Fig.10.2.21d**), was determined in the same way, and the results are presented in **Table 10.2.1**. The particle contained only pure copper, and its mass mCu was equal to $1.09412 \cdot 10^{-17}$ g. With these data, the composition and mass of the evaporated material of the nanoparticle were assessed. The calculations showed that the evaporated phase consists of both Ag and Cu with a mean composition of about 86 wt.% Ag and 14 wt.% Cu.It should be noted that a few nanometer-size particles, which are visible in the images (e.g. **Fig.10.2.21d**), resulted from a partial oxidation of Cu in the residual atmosphere of a TEM at a high temperature.

Our results revealed that intensive evaporation of the nanoparticles was activated at a temperature of 750°C, ultimately resulting in pure Cu remainders. Three options seem possible, namely, (i) sublimation of Ag from the alloy due to its lower vapor pressure as compared to Cu [3], (ii) congruent sublimation of AgCu alloy, and (iii) eutectic melting followed by evaporation of liquid phase.

Our assessments showed that the composition of the evaporating phase was about 86wt%Ag-Cu. This composition did not directly fit any of the abovementioned options. Nevertheless, our analysis showed that two evaporation processes occur simultaneously at this temperature, namely the primary one, which is forming a liquid phase at the specific surface planes of nanoparticle with subsequent evaporation, and the secondary one, which is sublimation of Ag.

1. Egerton, R. Electron Energy-Loss Spectroscopy in the Electron Microscope. Springer. 2011. https://doi.org/10.1007/978-1-4419-9583-4

2. Iakoubovskii, K., Mitsuishi, K., Nakayama, Y., Furuya, K. Mean free path of inelastic electron scattering in elemental solids and oxides using transmission electron microscopy: Atomic number dependent oscillatory behavior. Physical Review B. 2008, 77, 104102. https://doi.org/10.1103/physrevb.77.104102

3. Li, J.; Wang, Z., Li, Y.; Deepak, F.L. In Situ Atomic-Scale Observation of Kinetic Pathways of Sublimation in Silver Nanoparticles. Advanced Science. 2019, 6(8), 1802131. https://doi.org/10.1002/advs.201802131

10.2.6. Investigation of elemental partitioning and microstructural stability of 2nd and 4th generation SC superalloys during high-temperature ageing

Single crystal (SC) nickel-base superalloys are mainly applied as turbine blades and vanes in aero engines and industrial gas turbines. This group of alloys has been constantly developed for over 40 years to increase their superior mechanical properties, such as creep resistance and high-temperature strength. The Microstructure of SC superalloys consists of a high volume fraction of the hardening γ' phase, which are coherently precipitated in the γ matrix.

SEM microstructural examination was carried out using a Merlin Gemini II (ZEISS) microscope. TEM examination and Energy dispersive X-ray spectroscopy (EDX) analysis was carried out using TITAN G2 60-300 (FEI) equipped with ChemiStem system.

Ageing tests were performed on the samples of both generation superalloys, PWA 1484 and PWA 1497. The experiment aimed to investigate the high-temperature microstructural stability of both superalloys without external stresses. Four samples of each superalloy were isothermally aged at

temperatures 980 °C for 225, 450, 675 and 900 hours (with increasing time of exposure of 225 h step). **Figs 10.2.23** and **10.2.24** present SEM micrographs showing microstructure evolution during ageing of the PWA 1484 and the PWA 1497 superalloys, respectively.

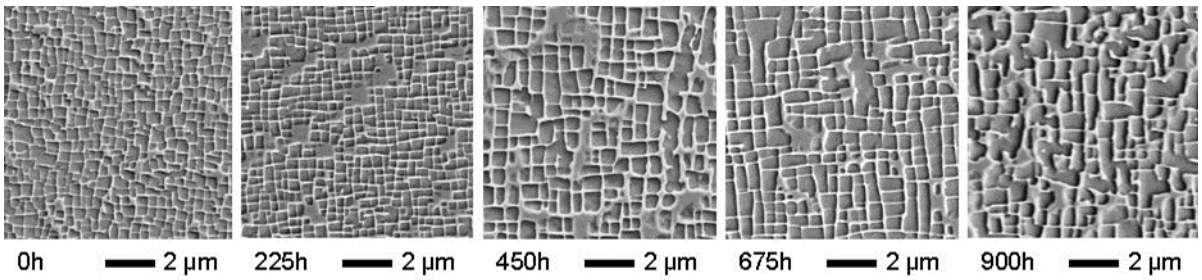

Figure 10.2.23. PWA 1484 superalloy microstructure evolution during ageing tests at 980 °C up to 900 h, showing coagulation of γ' particles and loss of cuboidal shape

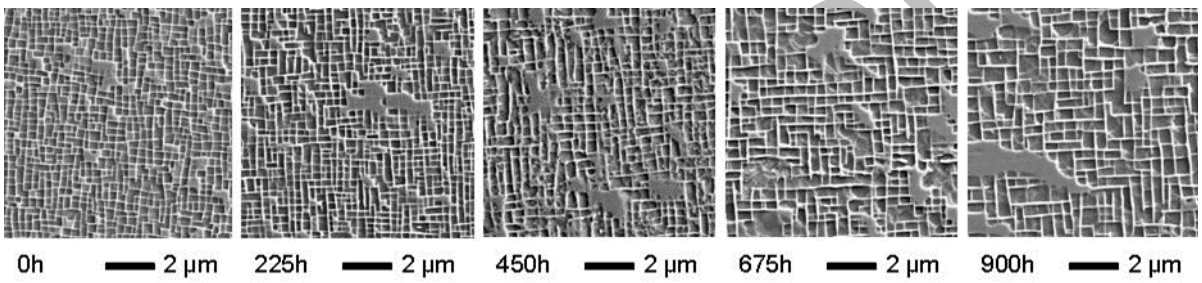

Figure 10.2.24. PWA 1497 superalloy microstructure evolution during isothermal ageing at 980 °C up to 900 h, showing coagulation of γ' particles but retaining them in a cuboidal shape

It was established that the matrix of 2nd generation PWA 1484 contains mainly Ni, Cr, Mo, W, Co and Re, while 4th generation PWA 1497 also contains Ru, Figs **10.2.25** and **10.2.26**.

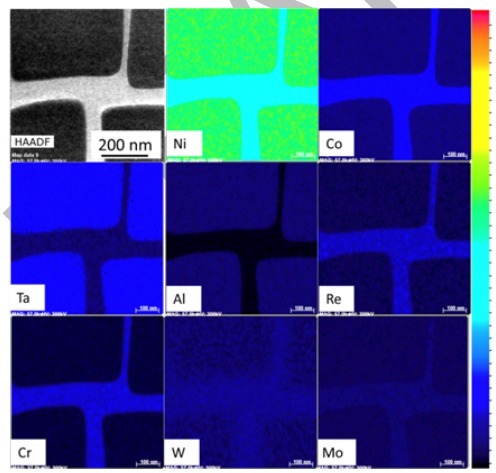

Figure 10.2.25. TEM-EDX elemental maps of PWA1484 as-received.

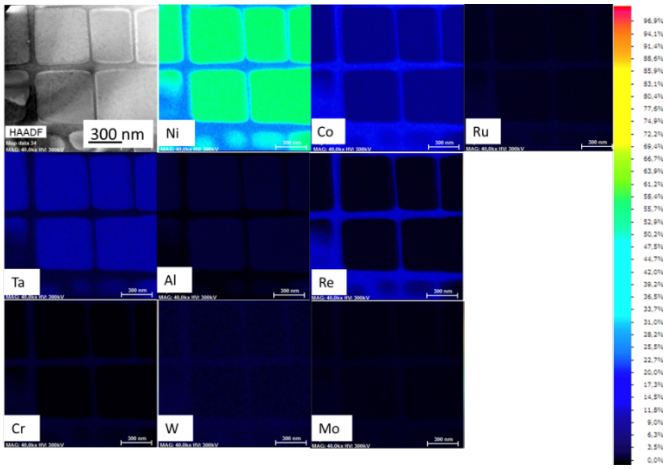

Figure 10.2.26. TEM-EDX elemental maps of PWA1497 as-received.

Task 10.3: Materials for Automotive Body and Chassis Structure (TRO, KRA, TOU)

10.3.1 Trends in heterogeneous nucleation of precipitates on α-dispersoids in Al-Mg-Si-Cu alloy with different heat treatment conditions (TRO, KRA)

This work is done by Dipanwita Chatterjee, Marius Andersen, Calin Marioara, Randi Holmestad, TRD –in collaboration with KRA

Heat treatment plays key role in precipitation strengthening of heat treatable Al-Cu-Mg-Si alloys. In this work, the effect of different cooling conditions, for example, air cooling and water quenching after solution heat treatment, followed by artificial ageing and natural ageing conditions was observed on nucleation and growth of Cu-containing secondary precipitates of Q' phase on the α-dispersoids using transmission electron microscopy (TEM), energy-dispersive X-ray spectroscopy (EDS) and FIB-SEM tomography techniques. Air cooling results in the growth of the secondary Q' precipitates more than water-quenching. This indicates that water-quenching condition results in alloys with higher strength. Using HR-STEM imaging and EDS spectroscopy, the segregation of Cu around the dispersoids was observed after 3 months of natural ageing in the water-quenched samples. In some of the secondary Q' precipitates, Cu-deficient structural arrangement of atoms or stacking faults was observed and its structure was investigated. Statistical estimate of the dispersoid density and volume fraction of the secondary precipitates for one of the air-cooled and artificially aged sample was investigated from TEM and FIB-SEM tomography datasets and compared. This resulted in precipitate and dispersoid statistics investigation from two different sample volumes and this investigation gives insight on the strengthening of the alloys.

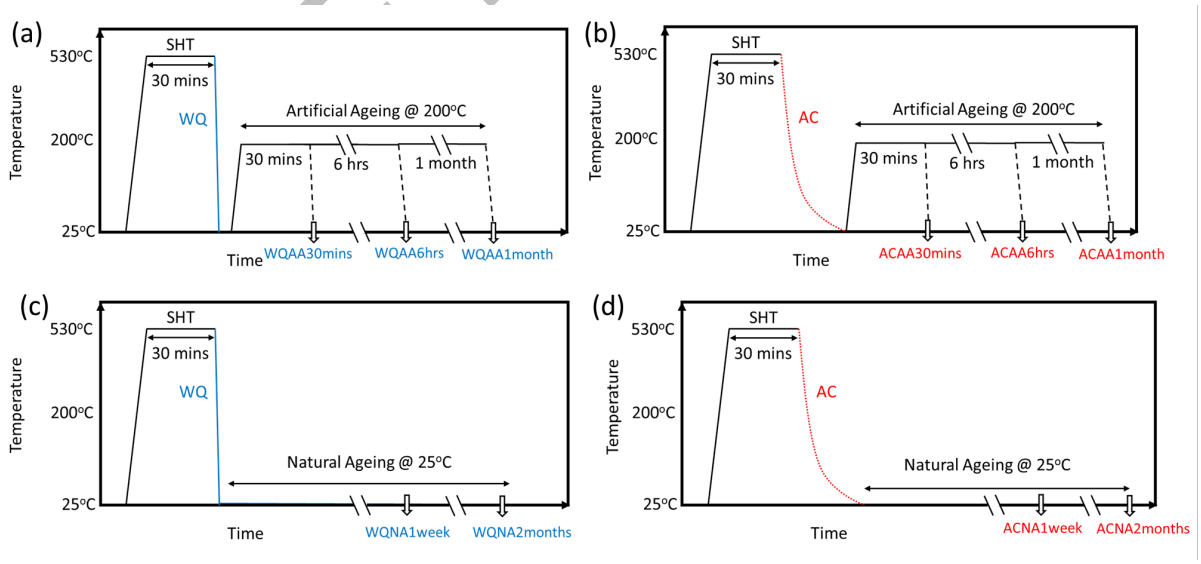

Figure 10.3.1. The different heat treatment conditions post SHT: air-cooled followed by artificial ageing, water quenched followed by artificial ageing, air-cooled followed by natural ageing and water quenched followed by natural ageing and the names of the samples are illustrated in the schematic.

The different heat treatments and the sample names are illustrated in **Fig.10.3.1.** The samples, heat treated differently were imaged to obtain statistics about secondary nucleation from about 30 dispersoids from each set.

Broadly, the air-cooled samples were observed to have large secondary precipitation on the dispersoids and the water quenched samples were observed to have much finer secondary precipitation on the dispersoids. **Fig.10.3.2** shows that air cooled samples in general have larger precipitates both in the matrix and on the dispersoids. The dispersoids have larger precipitate free zones around them. In some cases, there are still smaller secondary precipitates on the dispersoids. **Fig.10.3.3** shows that water quenched samples in general have smaller precipitates compared to air-cooled samples. With increase of ageing time, the size of the precipitates increases both in the matrix and on the dispersoid and the number of nucleation points on the dispersoids also increases. Precipitate free zones are smaller around the dispersoids.

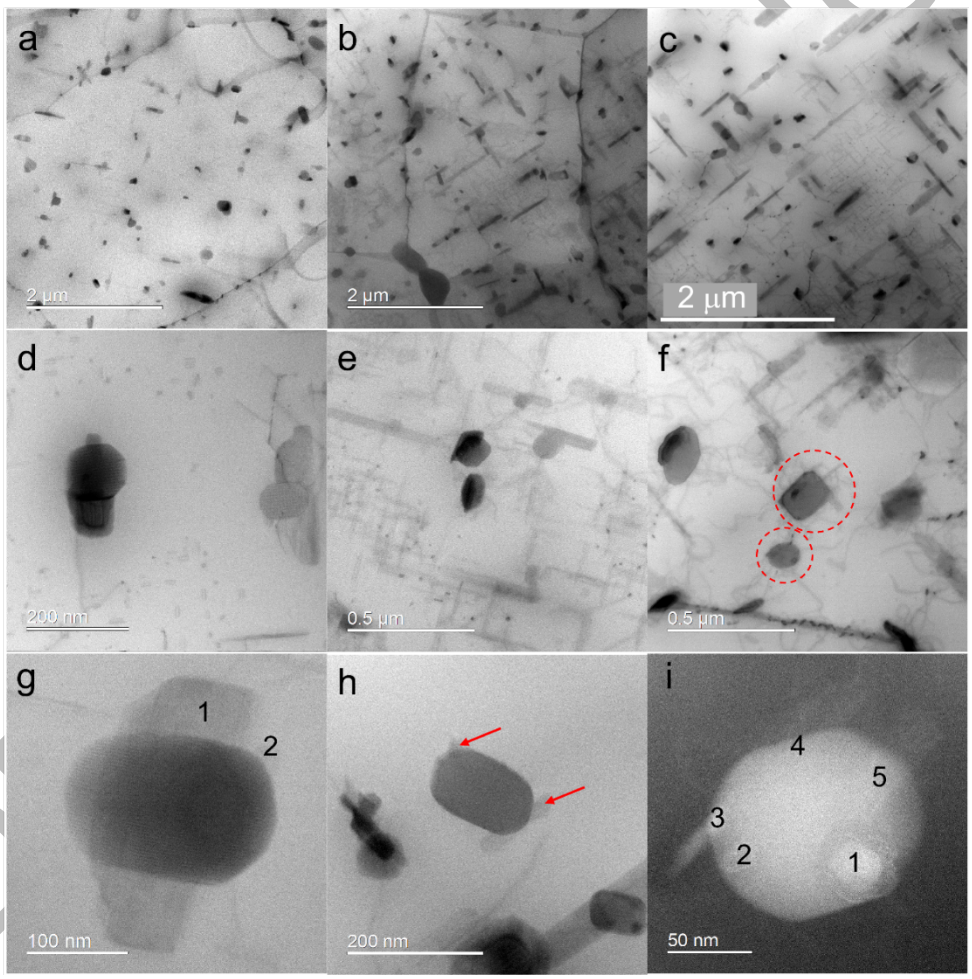

Figure 10.3.2. Ageing time series for air-cooled samples: a, b and c show low magnification overview images of the AC_AA_30mins, AC_AA_6hrs and AC_AA_1month samples respectively. The size of the secondary precipitates increase with increasing ageing time. Bright-field STEM images in d, e and f show closer view of individual dispersoids of the 3 conditions respectively. g, h and i show a more magnified view of the dispersoids. Several points of nucleation can be observed on each dispersoid at all conditions of ageing. Some dispersoids have smaller precipitates even at longer ageing times as marked with red circles and arrows in f and h. Closer view of secondary precipitates in 2(i) shows some of the smaller precipitates may be etched/cut during sample preparation.

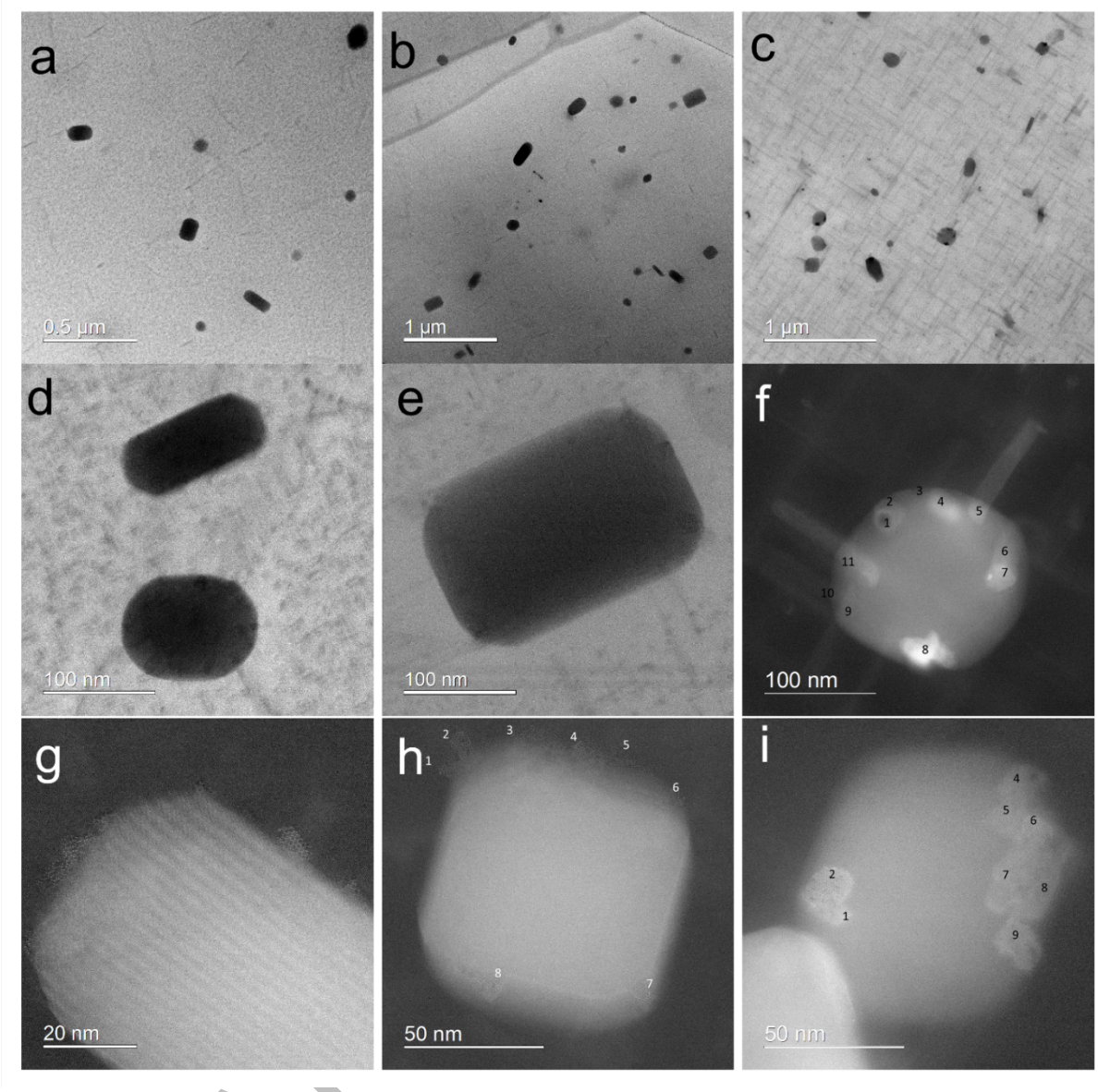

Figure 10.3.3. Ageing time series for water quenched samples show that with increasing ageing times, the precipitate size increases both in the matrix and on the dispersoids. The number of nucleation points also increase with increasing ageing times. The dispersoids have a relatively smaller precipitate free zone.

Natural ageing after water quenching shows segregation of Cu and Mg, the elements that constitute the precipitates, around the dispersoid. This was proved using EDS as shown in **Fig.10.3.4**. HRSTEM images of the surfaces of the dispersoids show a brighter contrast further providing evidence of Cu segregation.

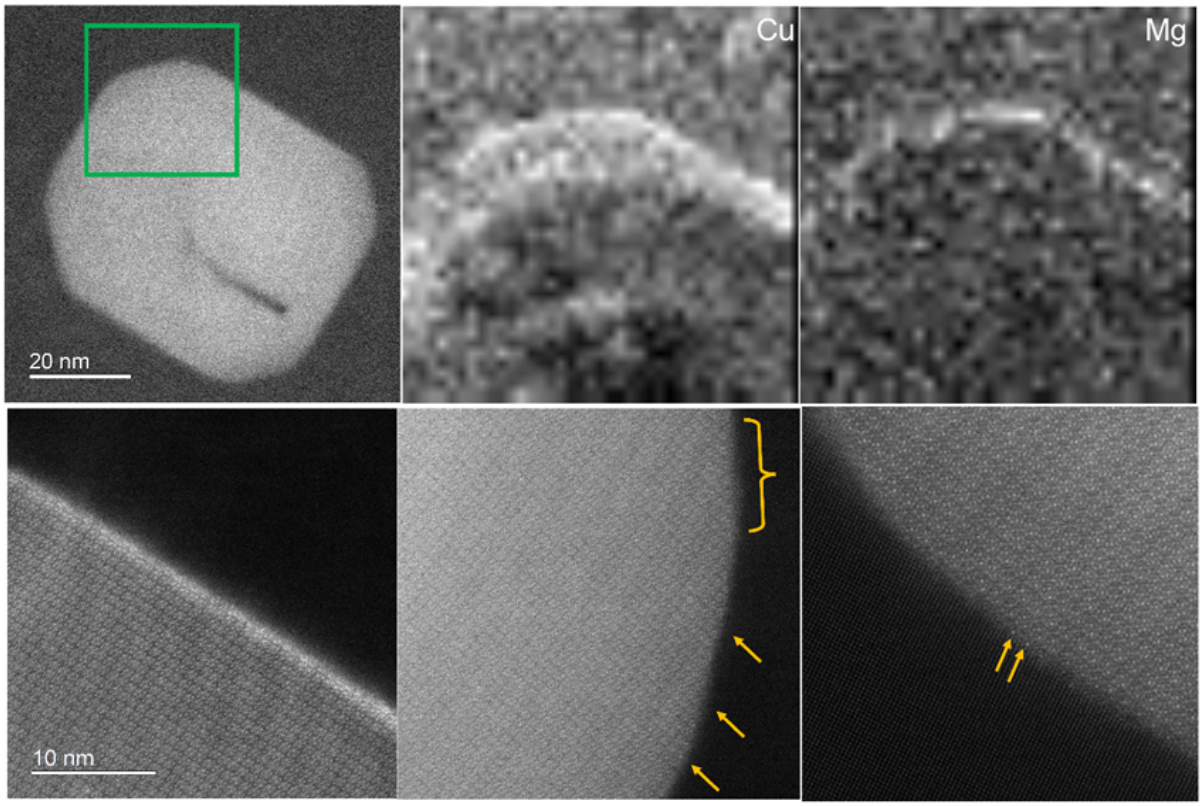

Figure 10.3.4. EDS mapping of the area marked in green shows natural ageing after water quenching shows segregation of Cu and Mg around the dispersoids. Bright contrast around the dispersoids in HRSTEM images also indicate probable segregation of high Z element Cu around the dispersoid.

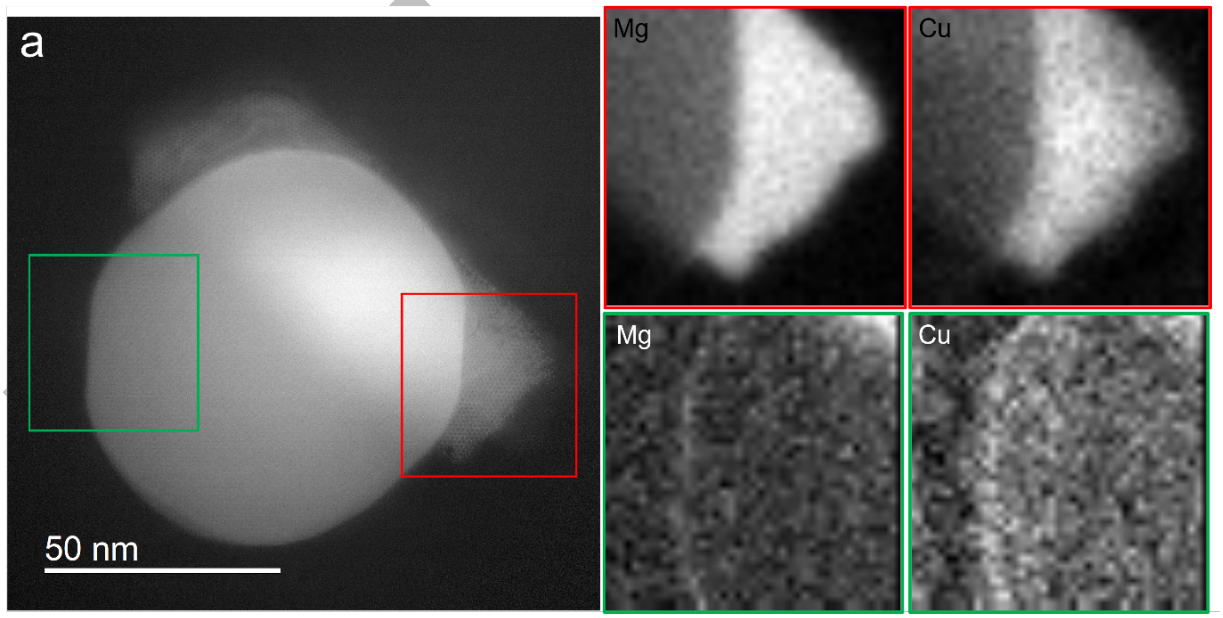

Figure 10.3.5. EDS mapping of the regions marked in red and green in natural ageing samples after air-cooling shows that even the surface of the dispersoid that do not clearly have precipitates indicate segregation of Cu and Mg on the surface of the dispersoids.

Naturally aged samples after both water quenching and air-cooling show segregation of Cu and Mg by EDS and HRSTEM imaging as shown in **Figures 10.3.4** and **10.3.5**. This indicates the starting point of nucleation of the secondary precipitates on the dispersoid surface.

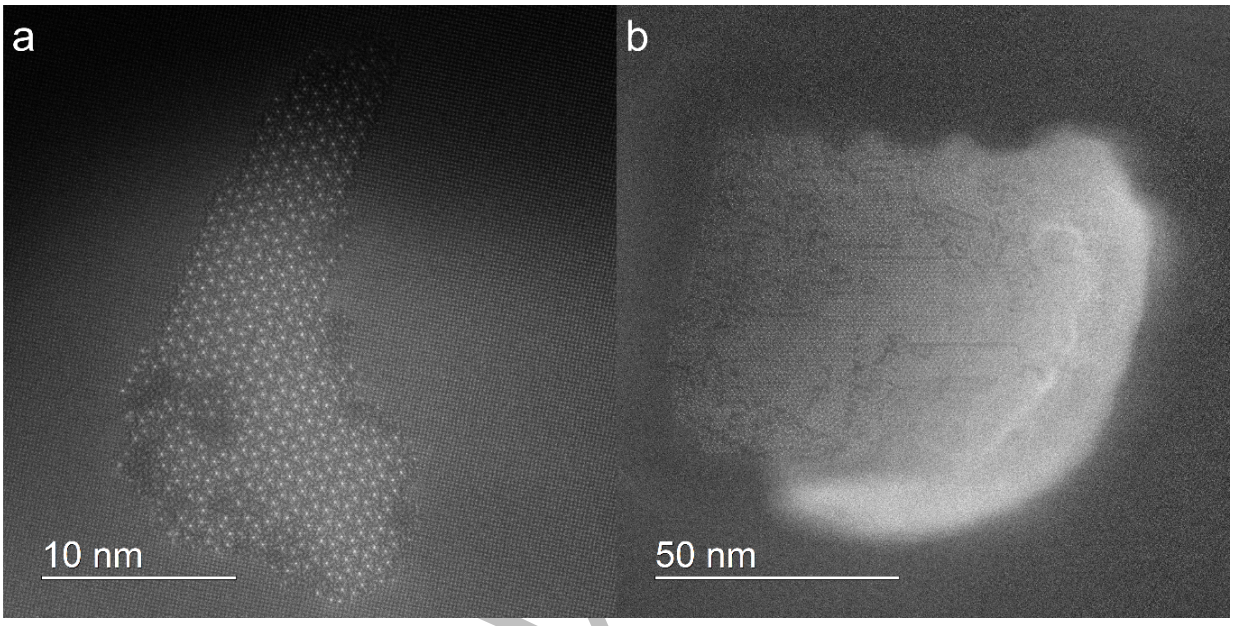

Figure 10.3.6. Defects in the secondary precipitate with areas deficient of bright Cu atoms

Secondary precipitates in most of the conditions were often observed to have defective structure with regions or channels of atoms deficient of Cu atoms as shown in **Figure 10.3.6**. The atomic structure of those defects was solved as shown in **Figure 10.3.7**.

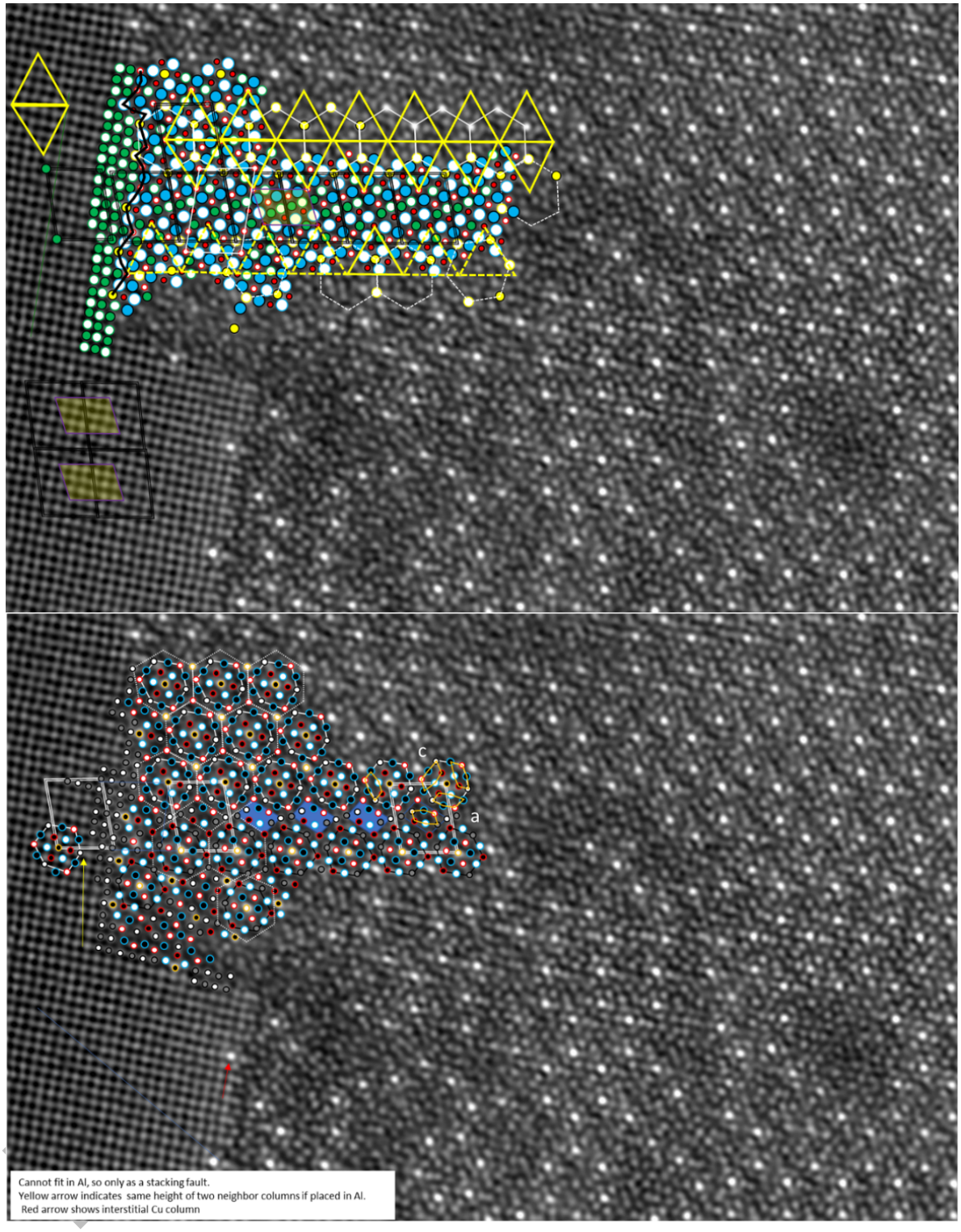

Figure 10.3.7. Elucidation of the structure of the stacking fault defect in the secondary precipitates on the dispersoids.

The structure will further be solved using Density Functional Theory (DFT) simulations. FIBSEM tomography experiments were carried out on the AC_AA_30mins sample to analyze the dispersoid number density, volume fraction of the secondary precipitates from a larger volume of the sample. This experiment was conducted by KRA and the data analysis was performed at TRO. **Figure 10.3.8** shows step by step data processing and segmentation of the precipitates and dispersoids based on the

shapes of the precipitates. Further refined segmentation needs to be performed in order to evaluate the volume fraction of the precipitates more accurately.

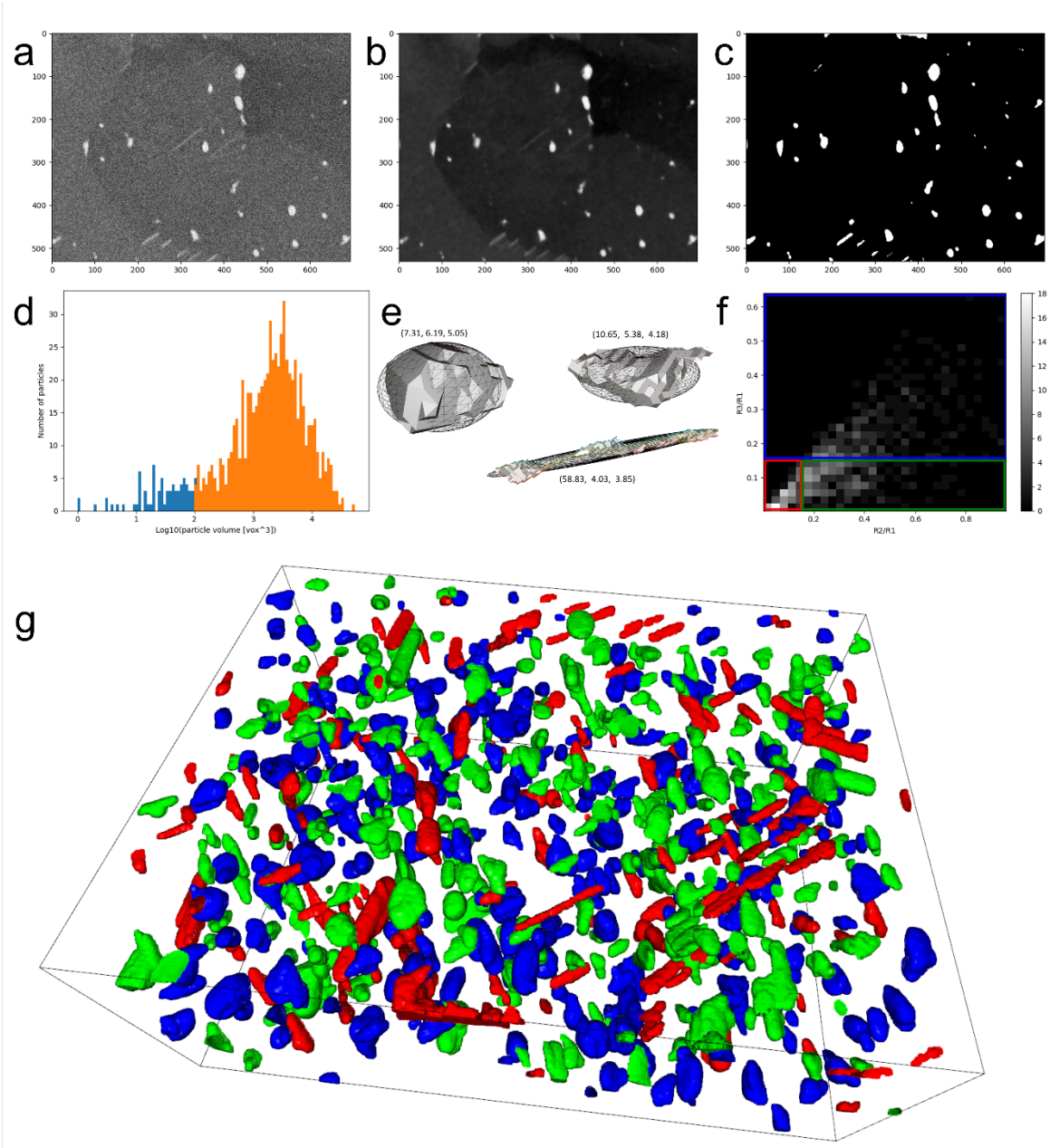

Figure 10.3.8. Analysis of the FIBSEM tomography data was done to segment the volume fraction of the secondary precipitate in the AC_AA_30mins sample.

Particle type	Count	Volume fraction [%]
Precipitates (red)	132	0.42
Dispersoids (blue)	278	1.00
Disc shaped (green)	277	1.55

Future work includes:

1. Solving the structure of atoms in the defect of the secondary precipitates
2. Segmentation of the secondary precipitates growing on the dispersoids in the FIB SEM tomography data analysis and more accurate volume fraction estimation
3. Comparison of the volume fraction of the precipitates estimated from TEM images and FIBSEM tomography data analysis

10.3.2. Data Analysis of Scanning Precession Electron Diffraction for Phase Mapping of Precipitates in Aluminium Alloys (TRD, CAM)

This work is done by Elisabeth Thronsen, Tina Bergh, Tor Inge Thorsen, Emil Christiansen, Jonas Frafjord, Ton van Helvoort, Randi Holmestad, TRD – in collaboration with CAM

Mapping the distribution of crystal phases is an important characterization task in multi-phase materials. Scanning precession electron diffraction (SPED) enables phase mapping of particles with nanoscale dimensions by collecting one precession electron diffraction pattern per probe position. To facilitate phase mapping, each diffraction pattern must be correctly labeled as its respective phase. We have tested four different data analysis approaches for phase mapping of embedded precipitates in an Al-Cu-Li alloy on a dataset containing three different crystal phases. The approaches include non-negative matrix factorization, template matching, vector analysis and artificial neural networks. A ground truth image was created from virtual images of the dataset and compared with the resulting phase map from each approach to estimate the accuracy. The accuracy, defined as the deviation from the manually determined ground truth image, was satisfactory for all approaches. For reproducibility of the approaches, the vector analysis performs best, since it requires less input from the user as compared to the other approaches. The codes for the different approaches will be openly available. The results are considered to be useful for phase mapping also in other material systems.

The SPED data set was acquired using a 2100F JEOL transmission electron microscope, operated at 200 kV, equipped with NanoMegas system ASTAR & Topspin and a Quantum Detectors Merlin camera. A precessing probe (~1 nm) was scanned across the specimen and acquiring one diffraction pattern at each position. This gave a 4D data set (x, y, k_x, k_y) consisting of a large stack of diffraction patterns.

A data set typically consists of up to of ~300 000 diffraction patterns, and we want an analysis method which is *open* (so we can understand, optimize and defend every step), *objective* (gives same answer for every user, as little pre-and post-processing as possible), *reliable* (gives correct answer every time) and *fast* (so large data sets can be analyzed). HyperSpy (https://hyperspy.org/) and Pyxem (https://github.com/pyxem/pyxem) are used in this work.

The material model system chosen was an Al-Cu-Li alloy with a nominal composition (in wt%) equal 3.00% Cu, 1.50% Li 0.55% Mn and 0.20% Fe, supplied by American Elements. The alloy was homogenized for 4 hours at 400°C, extruded, solution heat treated for 1 hour at 400°C, water quenched, naturally aged for 10 min at room temperature, and finally artificially aged for 24 hours at 250°C. The thermomechanical processing produced two distinct, co-existing precipitate phases, namely the hexagonal T1 (Al_2CuLi) and the tetragonal θ' (Al_2Cu) phase. Details of the three crystal phases (Al, θ' and T1) are given in **Figure 10.3.9**.

Aluminum matrix
Fcc; a=4.05 Å,
space group #225, Fm3m

T1 phase (Al_2CuLi)
hexagonal; a=b= 4.96 Å, c= 14.18 Å,
space group #191 P6/mmm.
Plates on $\{111\}_{Al}$ planes
$(001)_{T1} || (111)_{Al}$ and $\langle 110\rangle_{T1} || \langle 112\rangle_{Al}$

θ' phase (Al_2Cu)
tetragonal; a=b= 4.04 Å, c= 5.80 Å, space group #119, I4m2.
Plates on $\{001\}_{Al}$ planes
$(001)_{\theta'} || (001)_{Al}$ and $\langle 100\rangle_{\theta'} || \langle 100\rangle_{Al}$

Figure 10.3.9. Structure details, morphologies and orientation relationships of the three crystal phases in the data.

The T1 and θ' precipitates show different morphologies when viewed in projection along the ⟨001⟩Al zone axis and can therefore be distinguished based on their shapes in bright- or dark-field images. In total, six unique diffraction patterns were expected to appear in the SPED data from the Al [100] zone axis, as shown in **Fig.10.3.10**. Also, bright field and virtual dark field are shown here. Since the precipitate phases could easily be separated based on their morphologies, this enabled creation of a ground truth phase map shown in 10.3.10. The phase maps resulting from each phase mapping approach were then compared to the ground truth to determine the accuracy of the methods.

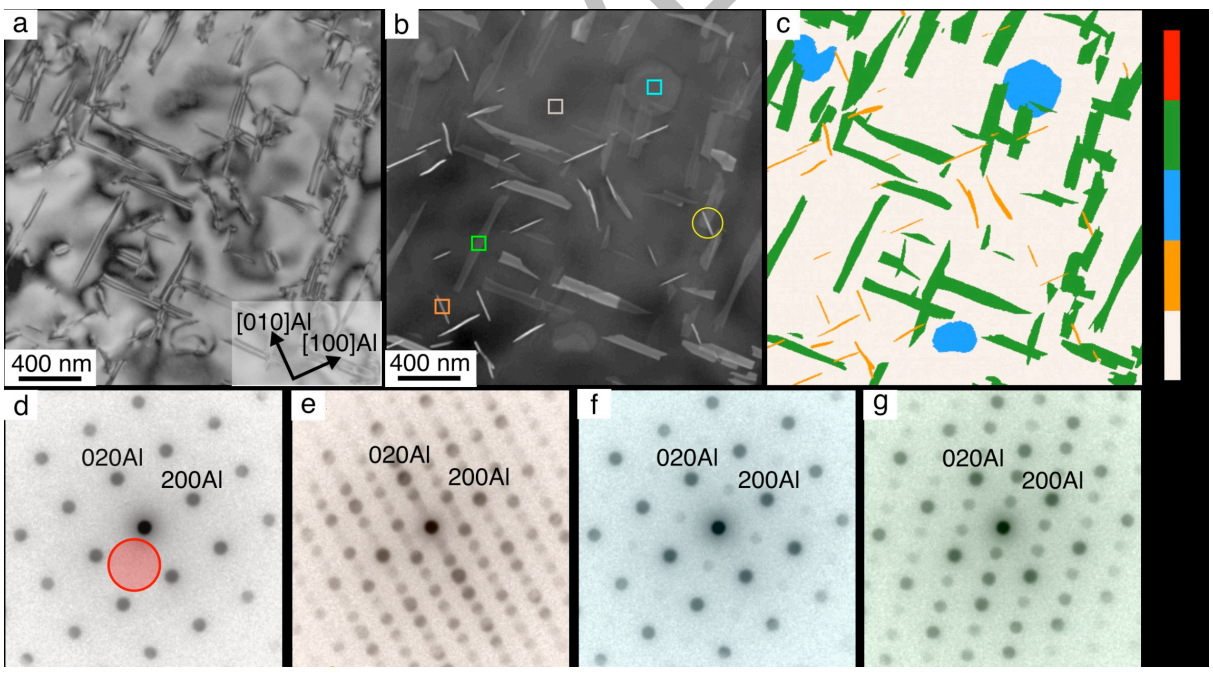

Figure 10.3.10. Overview over the dataset. A) Bright field image of the scanned region. b) Virtual dark field image of the dataset. The placement of the virtual aperture is indicated in (d). (c): The ground truth phase map. The coloured rectangles in (b) indicate regions where the experimental patterns in (d)-(g) were collected from, and correspond to Al, θ' ⟨100⟩, θ' ⟨001⟩ and T1, respectively. For clarity, the diffraction patterns are shown in log scale.

Four different analysis methods were tested and compared to ground truth. These were; 1) Non-negative matrix factorization (NMF); 2) Vector analysis; 3) Template matching and 4) Artificial neural network (ANN). Phase maps and difference maps for all the four approaches are shown in **Fig.10.3.11**. The difference maps were created by taking the difference between the ground truth in **Fig.10.3.10 c)** with the respective phase map obtained from the different approaches.

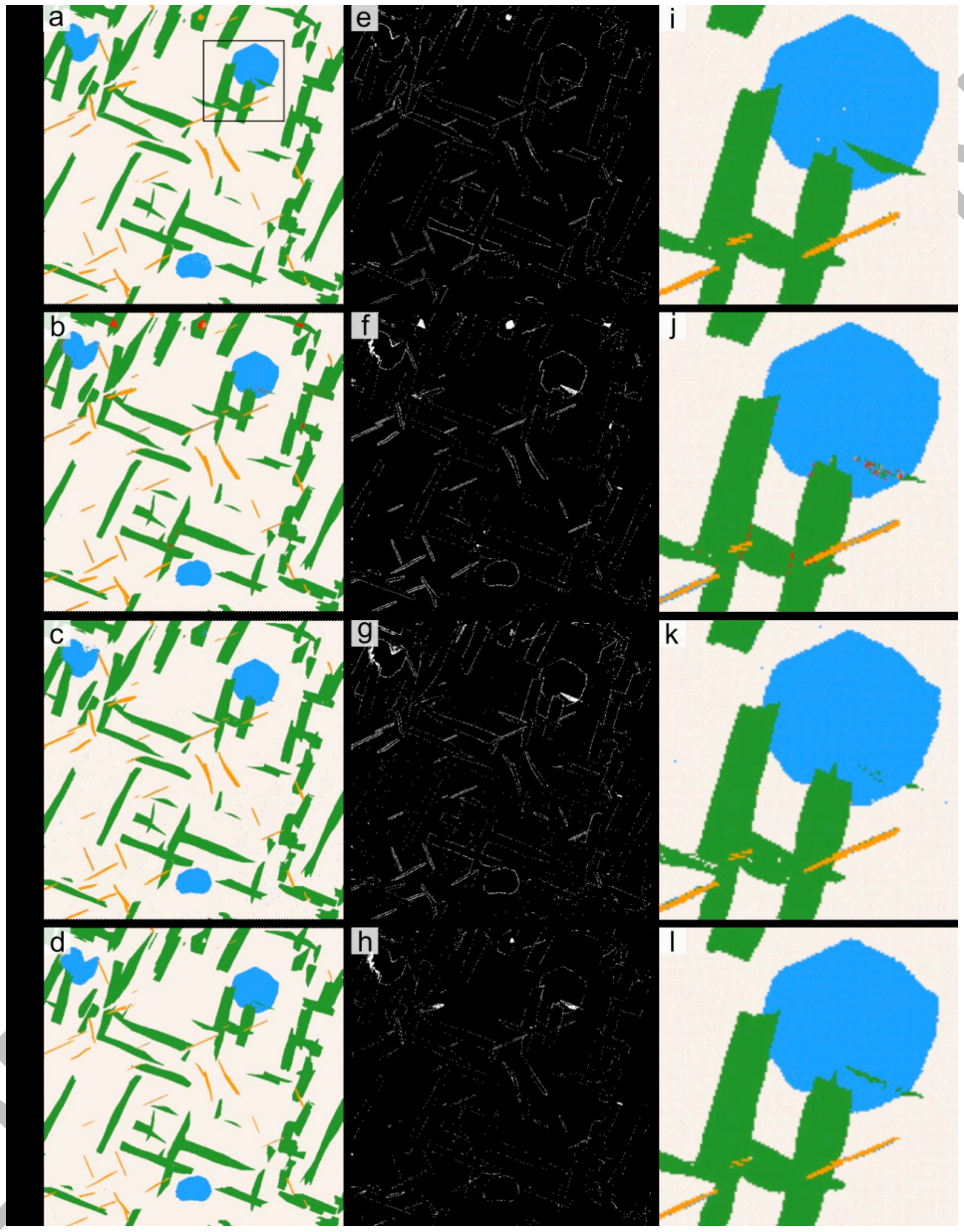

Figure 10.3.11. Phase maps and difference maps from the four phase mapping approaches. The difference maps were obtained by subtracting the respective phase maps from the ground truth, pixel by pixel. (a)-(d): Phase maps for NMF, vector analysis, template matching and ANN, respectively. (e)-(h): Difference maps for NMF, vector analysis, template matching and ANN, respectively. (i)-(l)): Enlarged regions corresponding to the rectangle in (a) of the phase maps in (a)-(d).

In general, the diffraction patterns stemming from precipitates show strong reflections from the Al matrix and weaker reflections from the precipitates. The precipitates exhibited different orientation relationships and morphologies, making them separable based on virtual imaging, enabling the

creation of a ground truth image used to estimate the accuracy of the phase mapping results. The phase mapping strategies included NMF, vector analysis, template matching and ANN, and they were compared based on accuracy and reproducibility. The main results are summarized as follows:

• All four phase mapping approaches work well on both weak and strong diffracted intensities and yield satisfactory accuracy with less than 2% of the pixels mislabeled. Most mislabeled pixels stem from regions at the interfaces between precipitate and Al.

• NMF has the advantage of reducing the dimensions of the dataset, and the resulting component maps generally have higher signal-to-noise ratio compared to the experimental diffraction patterns. The post-processing required to produce phase maps from NMF is subjective, and care should be taken upon analyzing the NMF components.

• The vector analysis is fast and accurate. It is also considered to be more objective as compared to NMF.

• The template matching requires the implementation of certain pre-processing steps such as background subtraction to increase the accuracy. The pre-processing is subjective, since the pre-processing approach and choice of parameters are user dependent. Upon using the same pre-processing and template library, the template matching is reproducible.

• ANN is considered to be an advantageous strategy in cases where multiple datasets with the same phases need to be classified since the classification itself is fast and accurate. The creation of training data is subjective and is considered to be the most tedious step. Once the ANN is trained, the results are reproducible.